JGR Oceans

RESEARCH ARTICLE
10.1029/2024JC021165

Deep Argo Observations of Antarctic Bottom Water in the Deep Fracture Zones of the Southwest Indian Ridge

Viviane V. Menezes[1], Pelle Robbins[1], Heather Furey[1], and Matthew Mazloff[2]

[1]Department of Physical Oceanography, Woods Hole Oceanographic Institution, Woods Hole, MA, USA, [2]Scripps Institution of Oceanography, San Diego, CA, USA

Key Points:

- The floats collected the region's largest temperature-salinity data set to date, with adjusted salinity meeting the Deep Argo target accuracy
- The floats found a new abyssal ventilation source (Novara fracture zone) to the Madagascar Basin and solved the Melville inflow puzzle
- The abyssal layer is fresher at the Melville fracture zone and saltier at Atlantis II, with Novara having intermediate water mass properties

Supporting Information:

Supporting Information may be found in the online version of this article.

Correspondence to:

V. V. Menezes,
vmenezes@whoi.edu

Citation:

Menezes, V. V., Robbins, P., Furey, H., & Mazloff, M. (2024). Deep argo observations of Antarctic bottom water in the deep fracture zones of the Southwest Indian Ridge. *Journal of Geophysical Research: Oceans*, *129*, e2024JC021165. https://doi.org/10.1029/2024JC021165

Received 30 MAR 2024
Accepted 5 JUL 2024

Author Contributions:

Conceptualization: Viviane V. Menezes
Data curation: Pelle Robbins
Formal analysis: Viviane V. Menezes, Pelle Robbins
Funding acquisition: Viviane V. Menezes, Heather Furey, Matthew Mazloff
Investigation: Viviane V. Menezes
Methodology: Viviane V. Menezes
Project administration: Viviane V. Menezes, Heather Furey
Resources: Viviane V. Menezes, Pelle Robbins, Matthew Mazloff
Software: Viviane V. Menezes, Matthew Mazloff

Abstract The Madagascar Basin is the primary pathway for Antarctic Bottom Water to ventilate the entire western Indian Ocean as part of the Global Overturning Circulation. The only way for this water mass to reach this basin is by crossing the Southwest Indian Ridge through its deep fracture zones. However, due to the scarcity of observations, the Antarctic Bottom Water presence has only been well-established in the Atlantis II fracture zone. In May 2023, the Deep Madagascar Basin Experiment deployed three Deep SOLO Argo floats in the exit of the fracture zones that were more likely to transport Antarctic Bottom Water: Atlantis II, Novara, and Melville. These floats have been collecting temperature and salinity profiles every 3–5 days with high vertical resolution in the deep ocean. In the present paper, we use the first 7 months of float data to characterize the Antarctic Bottom Water in the deep fracture zone area, revisiting a half-century puzzle about the Melville contribution. We also collected shipboard-based profiles to calibrate float salinity and show it is within the Deep Argo program target accuracy. We find Antarctic Bottom Water in both Melville and Novara fracture zones, not only in Atlantis II. This is the first time the Novara contribution has been revealed. The floats also uncover their distinct properties, which may result from the different mixing histories.

Plain Language Summary The Antarctic Bottom Water is important to the climate of our planet. It brings oxygen and other elements to the bottom of the ocean when it sinks around the Antarctic (thus its name) and moves north. However, we haven't had many ways to measure it until recently. Here, we use a relatively new technology called Deep Argo floats, which are autonomous robots that measure temperature, salinity, and pressure from the surface all the way down to the bottom of the ocean and transmit the data via satellite to land every few days when they are on the sea surface. We put three of these robots near the deep fracture zones of the Southwest Indian Ridge. The ridge is like a big wall separating two rooms, with the fracture zones being corridors in the wall that allow water in the ocean bottom to move from one room to the other. We chose corridors we guessed could have Antarctic Bottom Water: Atlantis II, Novara, and Melville. The robots are helping to solve a big mystery that has been around for 50 years and, in just 7 months of their 4-year missions, have already improved our understanding of the bottom of the ocean.

1. Introduction

Half a century ago, pioneering works from Warren (1974), Kolla et al. (1976), and Warren (1978) provided clear evidence of the presence of colder and fresher Antarctic-originated water in the bottom of the Madagascar Basin and suggested this as the primary route for the intrusion of Antarctic Bottom Water in the western Indian Ocean (Figure 1a). However, it is likely Le Pichon (1960) was the first to recognize the area east of Madagascar as a primary pathway, although inconclusively, as observations were too sparse, and the bottom topography was barely mapped. At these subtropical latitudes, Antarctic Bottom Water has been modified due to mixing with the overlaying Circumpolar Deep Water along the way (Gordon, 2019; Johnson, 2008; Orsi et al., 1999), and sometimes referred to as the Lower Circumpolar Deep Water (e.g., McCave et al., 2005). We prefer to use the Antarctic Bottom Water label for the bottom water as it reflects its formation area.

Over the years, our knowledge about the seafloor has improved significantly, providing a better understanding of the general routes of Antarctic Bottom Water from its formation regions around Antarctica (the Weddell Sea, Cape Darnley/Prydz Bay, Ross Sea, and Adélie/George V Land coast; Figure 1a) to northern latitudes as part of the deep limb of the global overturning circulation (e.g., Haine et al., 1998; Orsi et al., 1999; Silvano et al., 2023; Solodoch et al., 2022; van Sebille et al., 2013).

Supervision: Viviane V. Menezes
Validation: Viviane V. Menezes
Visualization: Viviane V. Menezes
Writing – original draft: Viviane V. Menezes
Writing – review & editing: Viviane V. Menezes, Pelle Robbins, Heather Furey, Matthew Mazloff

Due to the complex seafloor with shallow ridges and plateaus of less than 3,000 m depth, the only way for the Antarctic Bottom Water to reach the Madagascar Basin is by crossing the Southwest Indian Ridge (Arvapalli et al., 2022; Donohue & Toole, 2003; Kolla et al., 1976; Mantyla & Reid, 1995; McCave et al., 2005; Toole & Warren, 1993; Warren, 1974, 1978). The Southwest Indian Ridge, a mid-ocean ridge, separates the Crozet Basin (Southern Ocean) from the Madagascar Basin (Southwest Indian Ocean) with its meridionally oriented and narrow deep fracture zones (valley depths >4,000 m; widths of 20–40 km) connecting the two basins (Figure 1b) (Hosford et al., 2003; Patriat et al., 1997). As a result, the fracture zones are choke points for the Antarctic Bottom Water as the relatively shallow Madagascar and Crozet Plateaus on the west (45°E), the Southwest Indian Ridge on the south, and the Central Indian Ridge on the east (about 70°E) block its passage. The Crozet-Madagascar intersection accounts for half of the net deep (>3,200 dbar) northward transport of the Indian Ocean (Ganachaud et al., 2000). The other half is through the Perth Basin (southeast Indian Ocean).

It is fairly well documented that Antarctic Bottom Water flows equatorward through the Atlantis II fracture zone, whose northern end is at approximately 29.5°N and 57.5°E (e.g., Donohue & Toole, 2003; Kolla et al., 1976; MacKinnon et al., 2008; Mantyla & Reid, 1995; McCave et al., 2005; Swallow & Pollard, 1988; Toole & Warren, 1993; Warren, 1974, 1978). The Atlantis II fracture zone is characterized by an intense (10–30 cm/s) and thick (1,000 m vertically) northward jet, transporting 3 Sv of deep and bottom water and elevated mixing (10–100 $\times$ 10^{-4} m^2/s) (MacKinnon et al., 2008). MacKinnon et al. (2008) estimated that 20%–30% of the total meridional overturning circulation in the Indian Ocean occurs through the narrow Atlantis II, which makes this fracture zone a critical conduit for equatorward transport of bottom water in the global ocean.

The Antarctic Bottom Water presence in other deep fracture zones of the Southwest Indian Ridge is relatively unknown, despite early studies (Kolla et al., 1976; Warren, 1978) suggesting that the Antarctic Bottom Water also arrives in the Madagascar Basin between 60° and 64°E, where the Melville fracture zone is located (26°S; 61.33°E), and recent work (Arvapalli et al., 2022) shows Antarctic Bottom Water fingerprints in the Southwest Indian Ridge rift valley southeast this fracture zone (63°–69°E; 26°–27.5°S). The decadal-repeated hydrographic lines from GO-SHIP/CLIVAR/WOCE (Talley et al., 2016) are southward (I05S at 32–34°S), northward (I03 at 20°S), and westward (I07N at 54.5°E) of Melville, leaving a gap in observations and uncertainty about the Antarctic Bottom Water presence there. Whether or not Antarctic Bottom Water is exported from the Crozet Basin through the Melville fracture zone is an unsolved puzzle that has persisted for the last 50 years.

To obtain consistent thermohaline abyssal observations in this area, we deployed three Deep Argo floats as part of the Deep Madagascar Basin Experiment (DMB), which investigates the pathways of Antarctic Bottom Water toward and in the basin. These floats were deployed in May 2023 in the Antarctic Bottom Water potential arrival region (56°–61°E). Although it is not well-known in the physical oceanography community, between Atlantis II and Melville, there is another deep fracture zone called Novara (58.83°E; 28°S), more or less parallel to Atlantis II (Baines et al., 2007; Hosford et al., 2003; Patriat et al., 1997) and only discovered in 1980 according to the GEBCO Sub-Committee on Undersea Feature Names. Whether the Novara fracture zone is also a conduit for Antarctic Bottom Water toward the Madagascar Basin is another unresolved aspect of the Antarctic Bottom Water spreading puzzle. To detect the presence of Antarctic Bottom Water, we deploy one DMB float at the exit of each deep fracture zone in which Antarctic Bottom Water is likely to intrude (Atlantis II, Novara, and Melville). Hereafter, for clarity, we use the DMB acronym when related to our experiment and the Madagascar Basin for the geographic area.

Deep Argo floats are autonomous robotic platforms that measure thermohaline water properties over almost the entire water column in a much higher temporal resolution (days) (Zilberman et al., 2023) when compared with traditional shipboard observations (year-to-decades) (Talley et al., 2016). They are a relatively new technology aiming to expand the Argo mission to measure below 2,000 m, but no global Deep Argo array has been implemented yet (Johnson et al., 2015; Johnson & Lyman, 2014; Owens et al., 2022; Roemmich, Alford, et al., 2019; Zilberman et al., 2023). A fleet of about 1,200 deep floats is expected to be operational within 5–10 years and incorporated into the OneArgo design (Owens et al., 2022; Zilberman et al., 2023).

As proof of concept, regional pilot arrays of deep floats have been deployed in the Southern Ocean (Foppert et al., 2021; Thomas et al., 2020), Southeast Indian Ocean (Johnson et al., 2022; Tamsitt et al., 2019), Pacific Ocean (Gao et al., 2021; Johnson et al., 2019; Zilberman et al., 2020), and Atlantic Ocean (Desbruyéres et al., 2022; Johnson, 2022; Johnson & King, 2023). They are giving an unprecedented view of the abyss. However, none of these regional arrays focus on the Southwest Indian Ocean, and our floats are a small step in this direction.

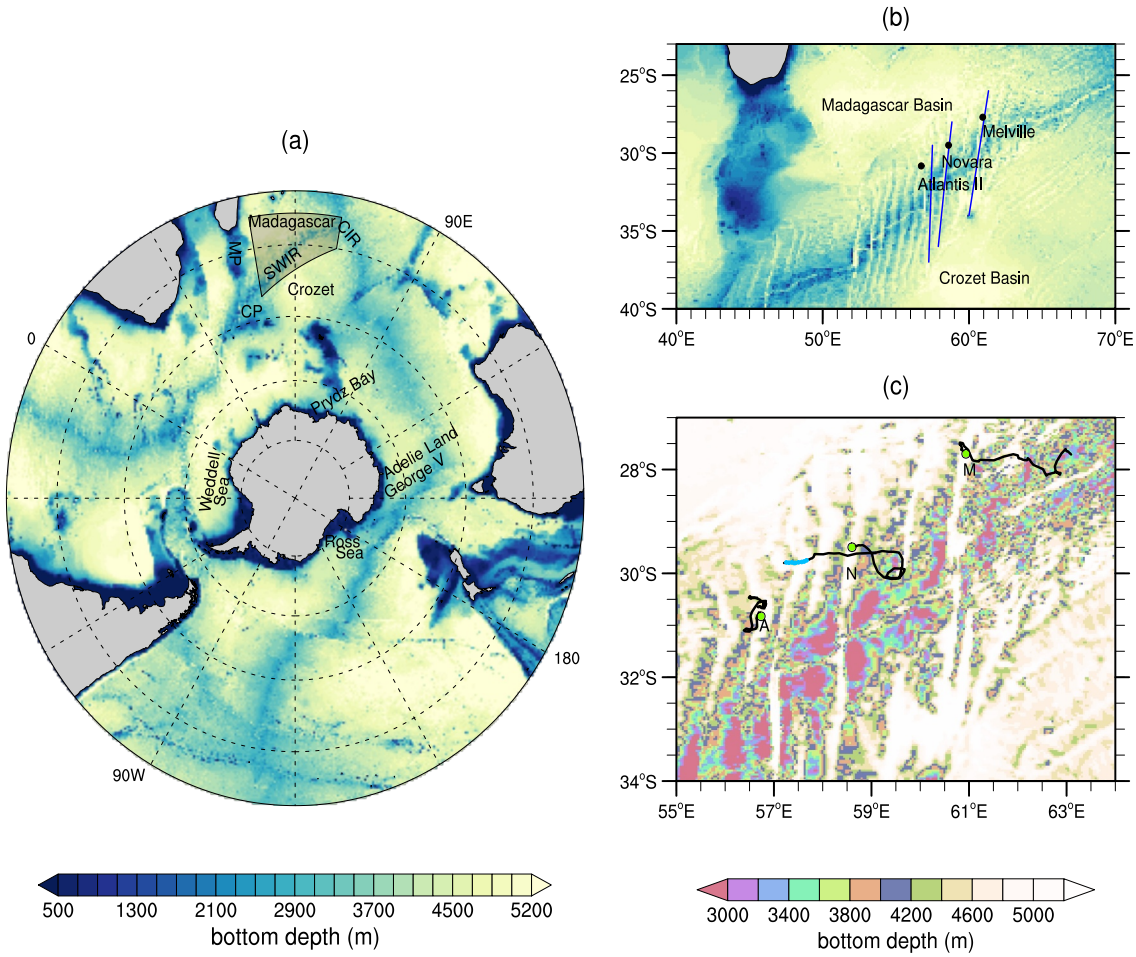

Figure 1. Bottom topography south of 20°S with main bathymetric features: (a) large-scale view; (b) Deep Argo float deployment positions (black dots) near three deep fracture zones (Atlantis II, Novara, and Melville) of the Southwest Indian Ridge; (c) float trajectories (black lines) overlaid to bottom topography (color). The topographic maps use reverse color schemes, such that deep features are mapped in light colors and shallow features in dark (navy blue in a and b or red in c). In (a): gray polygon highlights our region of interest. SWIR stands for Southwest Indian Ridge, CIR for the Central Indian Ridge, and MP and CP for the Madagascar and Crozet Plateaus, respectively. In (b): blue lines mark the fracture zones as determined by GEBCO (General Bathymetric Chart of the Oceans) Undersea Feature Names Gazetteer (https://www.ngdc.noaa.gov/gazetteer/). In (c): a non-sequential color map highlights the ridge and fracture zones, and *A*, *N*, and *M* labels identify trajectories from floats deployed near the Atlantis II, Novara, and Melville fracture zones, respectively. Green dots highlight the deployment positions. Cyan segment at Novara's float trajectory indicates when the float crossed the Atlantis II fracture zone exit. Bottom topography is from ETOPO (Earth TOPOgraphy)-2022 version 1 with 60 arc-s resolution (bedrock) (NCE, 2022).

Distinct from the pilot and future global arrays, the DMB floats are acquiring profiles at a much higher frequency (3–5 days) and with enhanced vertical resolution (5 dbar) in the deep ocean (>3,000 dbar). They are operating over rough topography (Figure 1c), where the global relief databases are not accurate at small scales, as we will describe later.

In the first 7 months of operation, 151 temperature and salinity profiles reaching below 3,000 dbar have been acquired in the region between 27.4°–31.2°S and 56.3°–63.1°E. This data set already contains the largest number of high vertical resolution CTD (Conductivity-Temperature-Depth) profiles in this region. Before the DMB float implementation, only three deep-reaching shipboard temperature and salinity profiles with high-vertical resolution (about 2 dbar) and 11 at low resolution (bottle data) were available in the World Ocean Database (version updated in November 2023) for the same area.

In the present paper, we use the first 7 months of data collected by these floats to characterize the Antarctic Bottom Water in the exit of the fracture zone of the Southwest Indian Ridge, revisiting the old puzzle about the Melville contribution (Kolla et al., 1976; Warren, 1974, 1978). We find Antarctic Bottom Water in both Melville and Novara fracture zones, not only in Atlantis II. To the best of our knowledge, this is the first time the Novara

Table 1
DMB Floats Deployed Near Atlantis II, Novara, and Melville Fracture Zones

Float	Atlantis	Novara	Melville
Number	1902474	1902475	1902476
Deployed on	02-May-2023	05-May-2023	07-May-2023
Latitude	30.8265°S	29.4879°S	27.6942°S
Longitude	56.7329°E	58.6132°E	60.9425°E
Local depth[a]	4,456 m	5,290 m	5,311 m
Cycles[b]	56	57	55
Meridional displacement[c]	76.09 km	72.61 km	71.02 km
Zonal displacement[c]	43.65 km	239.14 km	224.95 km
First deep cast (>3,000 dbar)[d]	6	5	6
Deep cast time in relation to the shipboard profile[d]	+2.05 days	+1.62 days	+2.28 days
Deep cast distance in relation to the shipboard profile[d]	9.43 km	11.45 km	5.15 km
Minimum pressure[e]	2,550 dbar	2,000 dbar	2,000 dbar
Optimized compressibility coefficient ($\times 10^{-8}$)	−12.316	−12.199	−12.037
Optimum cell gain M	0.9999	1	1

Note. Number is the respective World Meteorological Organization identifier; date, latitude, longitude, and depth refer to the deployment sites. [a]Measured during the accompanying shipboard casts. [b]Total number of profiles collected until 31 December 2023. [c]Meridional (latitude) and zonal (longitude) displacements are relative to the deployment positions and refer to the first 7 months of operation. [d]First cycle in which the float sampled below 3,000 dbar. Time and distance are relative to the accompanying shipboard cast. [e]Minimum pressure considered in the optimal estimation of the compressibility coefficient.

contribution has been revealed. The floats also uncover that the abyssal temperature-salinity (T-S) properties in each of these fracture zones are distinct. Specifically, the Melville abyssal layer is freshest, and Atlantis II is saltiest, with Novara in between. These differences are likely the result of distinct mixing histories of Antarctic Bottom Water with the overlying water.

The paper is organized as follows. Section 2 describes the DMB floats, including the setting and float operation, measurement accuracy, and the concurrent shipboard salinity profiles. Section 3 explains the calibration and adjustment of salinity data of the deep floats and describes the objective method used to analyze the water mass sources for the abyssal water in the region near the fracture zones. Section 4 presents the main results. These include comparisons of the deep float salinity with shipboard observations, showing the DMB float salinity observations have better than target accuracy, temperature and salinity data analyses, and a detailed view of water mass composition in the abyss. Section 5 provides a summary and conclusion.

2. Data

2.1. Deep Argo

The DMB floats are Deep SOLOs (Sounding Oceanographic Lagrangian Observer) from MRV Systems rated to 6,000 dbar (Roemmich, Sherman, et al., 2019). They were deployed in the Madagascar Basin near the northern end of three deep fracture zones of the Southwest Indian Ridge (valley depths >4,500 m): Atlantis II, Novara, and Melville, located on the ridge's central-eastern side (Figure 1b). By accident, during the DMB cruise, the Atlantis float was deployed 67.8 km west of the center of the Atlantis II fracture zone (Figure 1c), while the others were deployed as planned within the fracture zone exit. Table 1 gives deployment coordinates, dates, and local depth for the three floats. Hereafter, we refer to these floats as Atlantis, Novara, and Melville.

In Deep SOLOs, full water column temperature and salinity profiles are obtained in the descending instead of ascending phase (Roemmich, Sherman, et al., 2019). After reaching the profile target depth, the Deep SOLO climbs to the parking depth, drifting at this depth during a period determined by the user and then rising to the sea surface to transmit the data by Iridium short-burst data messaging (Roemmich, Sherman, et al., 2019).

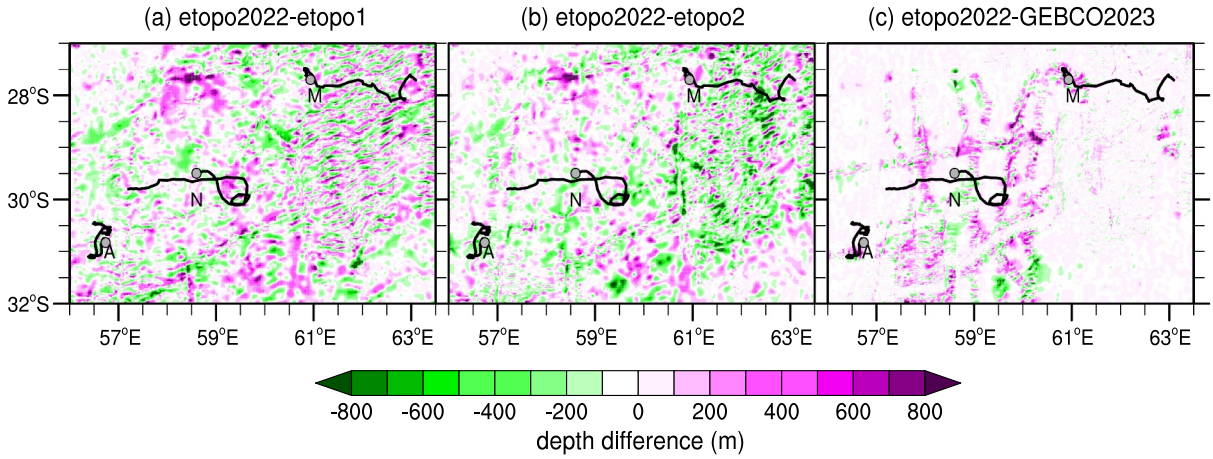

Figure 2. Local differences in seafloor depth between primary global relief data sets in the central-eastern Southwest Indian Ridge area: (a) ETOPO-2022 (NCE, 2022) minus ETOPO-1 (Amante & Eakins, 2009); (b) ETOPO-2022 minus ETOPO-2 version 2 (NGDC, 2006); (c) ETOPO-2022 minus GBECO-2023 (GEBCO Compilation Group, 2023). ETOPO-2022 and GBECO-2023 are available at 15 arc-s grid resolutions, while ETOPO-1 and are 1 and 2 arc-min resolutions, respectively. Higher resolution data sets have been linearly interpolated to lower for calculations. Black curves are the Deep Argo trajectories identified by *A*, *N*, and *M* labels for the Atlantis, Novara, and Melville floats, respectively. Gray dots mark the deployment locations. Positive values (pink) indicate deeper seafloor and negative values (green) indicate shallower seafloor.

Deep SOLOs are equipped with Sea-Bird SBE-61 CTD and use a passive bottom detection system consisting of a 3-m stainless steel wire attached to the float's bottom. For this CTD model, target accuracies are ±0.001°C for temperature (ITS-90, International Temperature Scale of 1990), ±0.002 for salinity (PSS-78, Practical Salinity Scale 1978), and ±4.5 dbar for pressure (Kobayashi et al., 2021; SBE, 2022), which are similar to the gold-standard shipboard GO-SHIP measurements (Hood et al., 2010; Katsumata et al., 2022; Talley et al., 2016). Comparisons with shipboard observations indicate that for pressure and temperature, the Deep SOLO measurements are within the target accuracy (Roemmich, Alford, et al., 2019). However, the salinity measurements have much higher uncertainty (0.004 PSS-78) than the target (Roemmich, Alford, et al., 2019; Wong et al., 2023).

The bottom detection system allows the float to get very close to the seafloor (for seafloor shallower than 6,000 dbar) while keeping the CTD at a safe distance from the bottom. This feature is critical in our study area because of its rough bottom topography (Figure 1c). Most of the regional Deep Argo arrays are implemented over flat abyssal plains. However, we are operating over inhospitable terrain that is not well mapped at small scales. Different global relief data sets such as the ETOPO and the GEBCO return bottom depths with hundreds of meters of difference at the same geographic coordinates in the Southwest Indian Ridge area (Figure 2). Even the most recent ETOPO-2022 (NCE, 2022) and GEBCO-2023 (GEBCO Compilation Group, 2023) products give bottom depths that disagree with float's depths by sometimes hundreds of meters, as shown later in Section 4.3. To mitigate this issue, we closely monitor the floats and adjust the profile target depths as frequently as appropriate. We take advantage of the Iridium communication that allows us to re-program the floats remotely when they are at the sea surface. In the first 7 months of operation, our floats have often touched the seafloor (black triangles in figures of Section 4.3), but no damage has been detected.

2.1.1. Configuration in the DMB Experiment

Since the DMB experiment aims for the floats to stay as long as possible in the fracture zone areas, we chose a parking level at 2,000 dbar, where currents are expected to be relatively weak in the region. This isobar corresponds to the lower limit of the subtropical gyre (Mantyla & Reid, 1995), and levels around it have been used as zero velocity surfaces (determined from water property distributions) for geostrophic calculations (e.g., Toole & Warren, 1993). Direct observations at the Atlantis II fracture zone show weak currents of a few cm/s at 2,000 dbar, intensifying downward and sustaining more than 30 cm/s at 3,500 m in a northward jet (MacKinnon et al., 2008, their Figure 2). The vertical structure of currents in the other fracture zones was unknown, and in the absence of direct measurements, we assumed they would resemble the ones at Atlantis II.

After 7 months of operation, the floats were still in the fracture zones area as planned. Relative to their deployment sites, they have displaced about 70 km in the meridional direction (about 0.6°) but with distinct zonal displacements. While the Atlantis float has moved less than 50 km in longitude, Novara and Melville floats moved more than 200 km zonally (Table 1), westward and eastward, respectively (Figure 1c). This indicates that the small-scale spatial variability in the circulation field at 2,000 m is larger than anticipated. Distances between deployment positions were 234.43 km (Atlantis and Novara floats) and 302.81 km (Novara and Melville).

A Deep SOLO takes about 13 hr to descend to 6,000 dbar and 17 hr to rise to the sea surface from a parking depth of 5,000 dbar (Roemmich, Sherman, et al., 2019). At the sea surface, it typically stays less than 10 min. For the DMB floats, the mean descending time to maximum depth is 10 hr, given that the bottom depths in our area are shallower than 6,000 dbar. For instance, the average maximum profile pressure in the first 7 months of operation is 3,830 dbar for the Melville float, 4,260 dbar for the Atlantis float, and 4,280 dbar for the Novara float. Time at the sea surface is the order of 12 min, and our floats take around 5 hr to rise from the parking depth at 2,000 dbar to the surface (and around 10 hr from maximum depth to parking depth).

Taking into account the temporal scales above and weighting the Deep SOLO battery life (expected to sample over 200–250 cycles) (Roemmich, Sherman, et al., 2019) and the aim to obtain the largest number of thermohaline profiles near the fracture zones as possible, we programmed our floats to collect profiles every 5 days instead of the typical 10-day cycle of the global Argo program. For the Novara float, we increased the temporal resolution between November 29 and 27 December 2023, when the float crossed the Atlantis II fracture zone exit (Figure 1c, highlighted in blue).

To conserve float battery, the Deep SOLO floats operate in dual sampling mode: continuous in the upper layer, when the float is descending most rapidly, and discrete at slower descent speeds in the intermediate and deep layers (Roemmich, Sherman, et al., 2019). Deep SOLO discrete default values in the deep ocean are 50-dbar between 3,000–3,800 dbar and 10-dbar below it. We used the default values for the first float cycles in May 2023 and cautiously increased the vertical resolution in the deep ocean (>3,000 dbar) first to 20 dbar and then 5 dbar (since 18 June 2023).

Deep SOLOs use a great deal of data compression, so the quantity of telemetry is small for the amount of data transmitted. The floats operating on the DMB mission generate 3.1 kB of telemetry per dive, leading to Iridium usage of about 20 kB/month.

2.2. Reference Salinity Profiles

Following the Deep Argo best practices (Walicka et al., 2022), shipboard CTD (SBE 9plus) measurements from the sea surface to 10 m above the seafloor were collected at the deployment positions after each float deployment. Original shipboard Practical Salinity (S_p) data were calibrated against samples from 24 Niskin bottles collected at discrete depths following GO-SHIP standard (Hood et al., 2010). Bottle salinities were measured by Guildline 8400A Autosal salinometers calibrated using the International Association for the Physical Sciences of the Oceans Standard Sea Water (Batch P-165). Final shipboard DMB data with a vertical resolution of 2 dbar have accuracies of 3 dbar for pressure, 0.002°C for temperature (ITS-90), and 0.002 g/kg for salinity on the absolute salinity scale (TEOS-10), same as GO-SHIP (Hood et al., 2010).

3. Processing

3.1. Deep Argo Salinity

3.1.1. Calibration

Accurate salinity measurements from Sea-Bird CTDs require a correction for the conductivity cell compressibility that occurs under increased pressure (Murphy & Martini, 2018; SBE, 2013; Zilberman et al., 2023). The degree of compressibility depends on the material used to manufacture the cell and the cell's geometry, and it is time-independent (Kobayashi, 2021; SBE, 2013). For SBE-61 model, Sea-Bird applies a default cell compressibility coefficient (CPcor) adjustment of -9.57×10^{-8} dbar^{-1}, inherited from the shipboard SBE-4 model, which uses a different cell encapsulant material (Roemmich, Sherman, et al., 2019; SBE, 2013). This value has been found too large for SBE-61, and as a result, the default Deep SOLO salinity measurements present a fresh bias when compared with shipboard observations—a bias that increases with increasing depth (Foppert

et al., 2021; Kobayashi, 2021; Kobayashi et al., 2021; Roemmich, Sherman, et al., 2019; Zilberman et al., 2019). Examples of these biases in the deep ocean are shown in Figure S1 in Supporting Information S1 (d-f, blue lines) for our floats.

Updated coefficient values for Deep SOLOs have been proposed and used to correct the pressure-dependence compressibility effect (Foppert et al., 2021; Johnson, 2022; Johnson & King, 2023; King et al., 2021; Kobayashi et al., 2021; Murphy & Martini, 2018; Roemmich, Sherman, et al., 2019; Thomas et al., 2020; Walicka et al., 2020, 2022; Zilberman et al., 2019, 2020). Currently, the Deep Argo community-recommended coefficient value for Deep SOLO real-time data is -12.5×10^{-8} dbar^{-1} (Wong et al., 2023). The U.S. Argo Data Assembly Center, which our floats are part of, automatically applies the community-recommended coefficient to obtain adjusted salinity values in real time in addition to the default salinity data that use the original Sea-Bird coefficient.

However, the best coefficient is dependent on the individual sensor, and improving the salinity accuracy involves having an optimized coefficient for each float, at least at this initial stage of Deep Argo floats (e.g., Kobayashi et al., 2021; Walicka et al., 2022). Different methods exist to estimate individual coefficient values (for instance, Foppert et al., 2021; Kobayashi et al., 2021; Walicka et al., 2022). Here, we use the best practice described in Walicka et al. (2022) and the Matlab code developed by Euro-Argo RISE partners (Wong et al., 2023), available on GitHub. The algorithm is based on the comparison of the float measurement with a reference in situ profile (Walicka et al., 2022; Wong et al., 2023) and consists of solving by least squares the equation below for the CPcor coefficient and optimum cell gain M:

$$C_e = \frac{C_{raw} \cdot M}{1 + \mathrm{CTcor} \cdot T + \mathrm{CPcor}_{opt} \cdot P} \quad (1)$$

where C_e is the conductivity estimated using a reference profile, C_{raw} is the raw conductivity data measured by the Deep SOLO without any pressure-dependence compressibility correction, M is a multiplicative calibration value, CTcor is the SBE-61 pressure-dependence canceling coefficient for temperature (3.25×10^{-6}) (Kobayashi, 2021; SBE, 2013), T is the in situ temperature (°C) measured by the Deep SOLO, CPcor_{opt} is the optimized pressure-dependent compressibility coefficient, and P is the in situ pressure (dbar) measured by the Deep SOLO. C_e is calculated based on the reference CTD practical salinity and Deep SOLO in situ temperature and pressure using the Gibbs-SeaWater Oceanographic toolbox (McDougall & Barker, 2011). $C_{raw} = a_1 C_o$, where a_1 is the coefficient to remove the original Sea-Bird correction from the default data ($a_1 = 1 + \mathrm{CTcor} \cdot T + \mathrm{CPcor\ (SBE)} \cdot P$, $\mathrm{CPcor\ (SBE)} = -9.57 \times 10^{-8}$) and C_o is the Deep SOLO conductivity obtained using Gibbs-SeaWater Oceanographic toolbox based on the default salinity, temperature and pressure measurements. Only data classified as good at real-time quality control processing by the Argo program and passed visual inspection were used in the optimization.

Our reference in situ profiles for the optimal estimations are the high-quality shipboard data collected after each float deployment (Section 2.2). The float data are from the first deep cast of the respective float, which in our case was obtained 1.6–2.3 days after the shipboard data and between 5.1 and 11.5 km distance (Table 1). This slight space-time mismatch occurs because the first few casts in the Deep SOLO are required to be shallow, progressively deepening toward the target depths (see Roemmich, Sherman, et al., 2019, for a full Deep SOLO operational description).

For the optimal estimation, we considered only the water column portion where salinity differences between Deep SOLO and shipboard data do not have large vertical gradients following the best practice described in Walicka et al. (2022). In our case, this layer is from about 2,000–2,550 dbar to the sea floor (Figure S1a–S1c in Supporting Information S1). We have also estimated optimal compressibility coefficients using other vertical layer definitions (not shown) to check the robustness and coefficient variations were within expectation (Wong et al., 2023). The optimal coefficient values used here are based on the thickest layer possible (Table 1).

We corrected the conductivity and calculated the corresponding practical salinity using the optimized coefficient and the optimum cell gain (Table 1 and Figure S1 in Supporting Information S1). Unlike Wong et al. (2023), here, we take into account the optimum cell gain to reconstruct the conductivity because it optimally corrects for an outstanding salty offset in the deep ocean observed in the Atlantis float (Figure S1d in Supporting Information S1,

pink asterisks). The community-recommended coefficient applied by the Argo Data Assembly Center also results in a similar offset (Figure S1d in Supporting Information S1, green circles), although the original Sea-Bird coefficient does not (Figure S1d in Supporting Information S1, blue circles). Calibrated practical salinity is then estimated from C_{cor} using Gibbs-SeaWater Oceanographic toolbox.

3.1.2. Further Adjustments

Density inversions are relatively common in CTD profiles and are generally associated with instrumental noise (Hood et al., 2010). In the case of the DMB floats, when we increased the vertical resolution of the discrete measurements to 5 dbar in the deep ocean, the lower part of the profiles (>3,000 dbar) became plagued with density inversions, in a level much more extensive (20%–35% of the deep measurements in each cast) than observed in the 2-dbar shipboard data from the DMB experiment and GO-SHIP hydrographic sections (4%–18%) or even in the DMB float casts with 20 dbar resolution (<10%). Investigations showed that the salinity measurements caused the unstable stratification, with all 5-dbar profiles presenting a quasi-regular step noise with a value of 0.001 in salinity. This small amplitude noise is not present in the temperature profiles.

In Deep SOLOs, measurements are compressed for data transmission. In that, Practical Salinity S_p is expressed in counts (integer numbers) and converted to scientific units during data processing as S_p = counts × gain—offset. Deep SOLO's default gain and offset for salinity are 1/1,000 and 1, respectively. The gain value means the effective Deep SOLO resolution for the salinity scale is 0.001 (three decimal places). However, the local vertical difference between discrete measurements taken at 5 dbar ($z_{i+1} - z_i$) in the deep ocean can be less than 0.001, as observed in the high-resolution shipboard data. These salinity variations (in the fourth decimal place) are truncated, resulting in noisy salinity profiles. In contrast, salinity differences taken over larger vertical distances (e.g., 20 dbar) tend to be above 0.001. Therefore, the truncation-related noise is not evident in the 20-dbar or 50-dbar salinity profiles.

To reduce the noise at 5 dbar profiles, we made small adjustments in salinity after the pressure-dependent compressibility correction had been applied. A similar adjustment is used to improve the salinity accuracy from animal-borne CTDs (Siegelman et al., 2019). The adjustment is based on the method developed by Barker and McDougall (2017) to stabilize hydrographic profiles. The premise is that temperature and pressure measurements are much more accurate than salinity, which is true for the Deep SOLO floats (Kobayashi et al., 2021; Roemmich, Alford, et al., 2019). The Barker-McDougall procedure consists of adjusting absolute salinity while keeping conservative temperature and pressure unchanged, such that the square of the buoyancy frequency (N^2) does not exceed a minimum threshold (here, defined as the default value, $N^2_{\min} = 1 \times 10^{-9} s^{-2}$). Absolute salinity and conservative temperature are variables from the TEOS-10 equation of the state of seawater and are calculated using the Gibbs-SeaWater Oceanographic toolbox (IOC et al., 2010; McDougall & Barker, 2011; McDougall et al., 2012). N^2 is also calculated using the same toolbox. Adjusted practical salinity is then obtained from the adjusted absolute salinity. To be consistent, we applied the Barker-McDougall procedure for all profiles, including the ones collected at lower vertical resolution in the deep ocean. The procedure reduced density inversions to about 10% or less in each cast.

3.2. Derived Variables

After calibration and adjustment of the salinity data, Deep SOLO profiles were interpolated into an evenly spaced vertical grid of 5 dbar resolution between the sea surface and the maximum depth measured by the respective float using a piecewise cubic Hermite polynomial, which preserves the curve shapes (Johnson et al., 2008). For each cast, no extrapolation outside the measured depth limits was allowed.

For clarity, we refer to the original float data as Level 0, the calibrated and adjusted data without interpolation as Level 1, and vertically gridded, calibrated, and adjusted data as Level 2.

For all levels, several variables have been derived, such as potential (θ) and conservative (Θ) temperatures, absolute salinity (S_A), and neutral density (γ). θ, Θ, S_A are from the TEOS-10 while γ definition is pre-TEOS10 (Jackett & McDougall, 1997) and an EOS80 (Equation Of Seawater 1980) legacy. Although we have used S_A for calculations using TEOS-10, all salinity plots in this study are expressed in PSS-78 as measured by Deep SOLOs.

Time-average temperature-salinity (θ-S_p) relationships have been determined based on the float's profiles. Mean θ-S_p curves were calculated on isotherms by averaging salinity. This was achieved by mapping the Level 2 data on

Table 2
Potential Temperature (θ) and Practical Salinity (S_p) for Three Water Types Used in the Optimum Multiparameter Analysis Representing the Antarctic Bottom Water, Circumpolar Deep Water, and North Atlantic Deep Water

Water types	θ [a]	S_p [a]
Antarctic Bottom Water	−0.753	34.660
Circumpolar Deep Water	0.650	34.707
North Atlantic Deep Water	3.280	34.921

[a]From Pardo et al. (2012).

vertical θ coordinates with a 0.05°C resolution using a piecewise cubic Hermite polynomial. The mean was only calculated if more than three measurements existed in the specific isotherm.

To determine when the floats descend the full water column and engage the passive bottom-detection device at the seafloor, we looked at the engineering portion of the telemetry message. The float transmits a flag to indicate when the float's descent is stalled at the deepest point. Combining the flag status with the measured descent velocity allows us to distinguish between a float descent terminated by encountering the seafloor versus a descent that ends with the float neutrally buoyant in the water column short of the full depth.

3.3. Quantifying Water Mass Sources for the Abyssal Water

We used an optimum multiparameter analysis to quantify the relative contributions of water masses for the abyssal water (>3,000 dbar) in the Southwest Indian Ridge area (see Tomczak & Large, 1989, for a detailed explanation about this method). The basic idea is that conservative tracers such as temperature and salinity in the ocean interior result from mixing from well-defined source water masses, that is, there is no external source or sink of properties (e.g., Johnson, 2008; Pardo et al., 2012; Tomczak & Large, 1989). In this method, mixing is represented by linear combinations of water types, which are unique points in the parameter space. A water type (mathematical representation) should not be confused with a water mass that is a body of water with a common formation history, occupying a volume in space and defined by ranges in water properties (Tomczak & Large, 1989). Here, we use this water mass decomposition method to provide a first-order description, but more sophisticated inverse-method approaches exist (e.g., Gebbie & Huybers, 2010).

In the Southwest Indian Ocean, abyssal water below 3,000 dbar is influenced by three major water masses, namely the Antarctic Bottom Water, Circumpolar Deep Water, and North Atlantic Deep Water, in which Antarctic Bottom Water is the densest (lower abyssal layer) and North Atlantic Deep Water the lightest (upper abyssal layer) (Donohue & Toole, 2003; Johnson, 2008; Mantyla & Reid, 1995; Toole & Warren, 1993; van Aken et al., 2004; Warren, 1978; You, 2000). In our analysis, we consider water types that represent these water mass sources (Table 2), although Circumpolar Deep Water is already a mixture of several deep and intermediate water masses, which includes North Atlantic Deep Water and Antarctic Bottom Water (Rintoul et al., 2001). Because of that, Johnson (2008) chose to consider only the ventilated North Atlantic Deep Water and Antarctic Bottom Water in their optimum multiparameter analysis of the global oceans. Our analysis explicitly takes into account Circumpolar Deep Water because we are interested in determining the extent to which the abyssal water in the Southwest Indian Ridge area is closer to pure Antarctic Bottom Water and mixed Circumpolar Deep Water.

A water mass not considered here is the (North) Indian Deep Water (Park et al., 1993; Toole & Warren, 1993; van Aken et al., 2004; Warren, 1981; You, 2000) given the large uncertainties surrounding it. The Indian Deep Water is a saline and diffusely formed water mass lying typically above the North Atlantic Deep Water (Talley, 2013). Its spreading pathways in the South Indian Ocean are conflicting in the literature (e.g., McCave et al., 2005; Toole & Warren, 1993; van Aken et al., 2004; Warren, 1981; You, 2000), and water mass characteristics are not easily pinpointed in a temperature-salinity diagram. While You (2000) describe the Indian Deep Water as aged Circumpolar Deep Water, van Aken et al. (2004) consider it an ancient form of North Atlantic Deep Water, and Talley (2013) also indicates that Antarctic Bottom Water is part of its composition; thus, the Indian Deep Water is connected to Circumpolar Deep Water, North Atlantic Deep Water, and Antarctic Bottom Water considered here, which are easily recognized as sources below 3,000 dbar in the latitudes sampled by the DMB floats.

Since our Deep SOLOs measure temperature and salinity, our water types are defined only by these parameters (Table 2). This approach is similar to the one employed by Thomas et al. (2020) in their optimum multiparameter analysis of Deep Argo data in the Antarctic-Australian Basin. To define the water type properties, we rely on the work of Pardo et al. (2012), which determined them based on the GLODAP (Global Ocean Data Analysis Project) and CARINA (CARbon dioxide IN the Atlantic Ocean) data syntheses. Implicitly, we are assuming a steady state where water source properties do not change over time.

Considering three water types and assuming conservation of mass, one can write the mixing equations as follows:

$$x_1\theta_1 + x_2\theta_2 + x_3\theta_3 + n_\theta = \theta_{obs} \tag{2}$$

$$x_1 Sp_1 + x_2 Sp_2 + x_3 Sp_3 + n_{Sp} = Sp_{obs} \tag{3}$$

$$x_1 + x_2 + x_3 + n_m = 1 \tag{4}$$

where subscripts 1 to 3 represent a water type (Antarctic Bottom Water, Circumpolar Deep Water, and North Atlantic Deep Water), x is the respective fraction of water type in the mixture, θ and Sp are the water type potential temperature and practical salinity, respectively, n_* represent the respective uncertainties associated to each variable, and $*_{obs}$ are the observed values. Here, the linear system above is solved by weighted and tapered least squares whose solutions (Wunsch, 1996) are:

$$\widetilde{\mathbf{x}} = \left(\mathbf{H}^T\mathbf{R}^{-1}\mathbf{H} + \mathbf{P}^{-1}\right)^{-1}\mathbf{H}^T\mathbf{R}^{-1}\mathbf{y} \tag{5}$$

$$\widetilde{\mathbf{n}} = \mathbf{y} - \widetilde{\mathbf{x}} \tag{6}$$

where $\widetilde{\mathbf{x}}$ and $\widetilde{\mathbf{n}}$ are water mass fractions and residual estimations, respectively, $\mathbf{H}$ represent the water type properties, $\mathbf{P}$ error variance associated to the water types and $\mathbf{R}$ error variance of the measurements. Distinct from some other implementations of the optimum multiparameter analysis (e.g., Johnson, 2008; Pardo et al., 2012; Tomczak & Large, 1989), we did not impose nonnegativity constraints on the solutions.

Water-type properties can assume distinct values, as water masses are typically defined within a range. For instance, Johnson (2008) defines Antarctic Bottom Water water type with $\theta = -0.88$ and $S_p = 34.641$ while in Pardo et al. (2012), it is slightly warmer and saltier (Table 2). Moreover, the error variances associated with the measurements ($\mathbf{R}$) and water types ($\mathbf{P}$) need to be known or prescribed. To deal with these uncertainties, we solved the system using many combinations of water-type definitions and measurement error variances. However, we kept the error variances on water masses ($\mathbf{P}$) to equal proportions for all combinations. Since differences between Johnson (2008) and Pardo et al. (2012) definitions are around ± 0.1 in θ and ± 0.02 in S_p for a given water mass, we considered multiple values in these ranges for each water type using the values shown in Table 2 as central values. For the error variances of the measurements, we considered values between 0.7 and 1.2 standard deviations for both potential temperature and salinity. Values below 0.7 standard deviations tended to give solutions with predominantly negative contributions for the Melville float data. For instance, when we used 0.6 standard deviations for those data, only 10% of the solutions were predominantly positive (≥95% of the float data). Table S1 in Supporting Information S1 gives the standard deviation below 3,000 dbar considered here for each DMB float. In physical units, error variances varied from 0.16°C to 0.38°C for potential temperature and from 0.005 to 0.013 for salinity.

We solved the above system using 2,700 distinct combinations of water types and error variances on measurements and averaged the solutions for each float to obtain the water mass source fractions. Only combinations in which $\widetilde{\mathbf{x}}$ were primarily positive (i.e., combinations in which water mass fractions were positive at more than 95% of the respective float data) were used to build the ensemble means. For the Melville float, 1,844 combinations met this criterion, whereas all met it for the Atlantis and Novara floats. The remaining negative values were small and randomly distributed and not considered in the averaging process. The standard deviations in the ensembles are relatively low, less than 6%, with the highest variability found for the Circumpolar Deep Water and lowest for North Atlantic Deep Water (Figure S2 in Supporting Information S1). Mass residuals are overall low and decrease in the water column, with Melville float presenting the highest values in general (0.096, Figure S3 in Supporting Information S1). Given the accuracy of Melville's float measurements is similar to Atlantis and Novara data, as we show in Section 4.1, it is possible that the Melville float is under the influence of additional deep water mass sources such as the Indian Deep Water, not considered in our water mass decomposition, which may explain the differences described here.

Following Johnson (2008), for each cast, the ensemble-mean fractions of Antarctic Bottom Water, Circumpolar Deep Water, and North Atlantic Deep Water were depth-integrated to give the equivalent water-class thickness.

Table 3
Deep SOLO Skill in Retrieving (Practical) Salinity[a] in the Deep Ocean (>3,000 dbar) in the Southwest Indian Ridge Area for Floats Deployed Near Atlantis II, Novara, and Melville Fracture Zones

	Product[b]	Coefficient[c]	Atlantis	Novara	Melville
bias[d]	Level 1	Optimized	0.0001	0.0004	9.3×10^{-6}
	Level 0	Community-recommended	0.0042	0.0009	0.0006
	Level 0	SBE	0.0003	−0.0031	−0.0034
rmsd[e]	Level 1	Optimized	0.0007	0.0009	0.0004
	Level 0	Community-recommended	0.0043	0.0011	0.0007
	Level 0	SBE	0.0009	0.0033	0.0034
range(Δ)[f]	Level 1	Optimized	[−0.0008 0.0015]	[−0.0009 0.0025]	[−0.0007 0.0010]
	Level 0	Community-recommended	[0.0033 0.0056]	[−0.0006 0.0028]	[−0.00001 0.0015]
	Level 0	SBE	[−0.0011 0.0021]	[−0.0051 −0.0007]	[−0.0042 −0.0019]

Note. Statistical comparisons are between the first deep cast[g] of the respective float and the CTD taken after their deployments (see Table 1). [a]Practical salinity uses PSS-78. [b]Product refers to the Deep SOLO processing level (Section 3.2). [c]Pressure-dependent compressibility coefficient used in the product (Section 3.1.1). [d]Mean difference in salinity below 3,000 dbar. Differences were calculated as $\Delta(\theta) = float(\theta) - ctd(\theta)$ in coordinates of potential temperature (θ); thus, positive values mean float data are saltier and negative fresher. [e]Root-mean-square of the differences. [f]Minimum and maximum differences. [g]First deep casts have discrete measurements every 50 dbar below 3,000 dbar.

For the water mass mixing analysis, we use the Level 2 (calibrated and adjusted) data from Deep SOLOs below 3,000 dbar. Observations and water-type properties have been normalized by the mean and standard deviation of observations (Table S1 in Supporting Information S1) prior to analysis.

4. Results

4.1. Salinity Accuracy

While Deep SOLO floats are known to measure temperature and pressure within the target accuracy below 2,000 dbar, the same has yet to be reached for salinity (Roemmich, Sherman, et al., 2019; Zilberman et al., 2023). Here, we present some statistics comparing our Deep SOLO salinity data to the accompanying shipboard CTDs, showing that our Level 2 salinity observations are indeed within the target accuracy. Our focus is on the abyssal ocean below 3,000 dbar, where we can find Antarctic-originated water. As in Kobayashi et al. (2021), comparisons were performed on isotherms, with the generally accepted assumption that temperature and pressure sensors in the floats are more accurate than salinity. Comparisons on isotherms also minimize the effects of short-term heaving as our floats' first deep casts are not from the exact same place and time (Table 1). For the comparisons, the high vertical resolution shipboard CTD profiles have been mapped on the respective float isotherms. The float first deep casts have a vertical resolution of 50 dbar in the deep ocean (Section 2.1). We evaluate the bias (i.e., the mean difference below 3,000 dbar), the root-mean-square of the differences, which can be interpreted as an error measurement, and minimum/maximum differences in the deep ocean (Table 3).

After calibration, salinity bias and root-mean-square of the differences are reduced in all floats compared to Level 0 data using either the community-recommended or the original Sea-Bird coefficient (Table 3). This improvement is particularly noticeable for the Atlantis float, where the community-recommended coefficient results in a salty bias of 0.004 (PSS-78, hereafter) compared with 0.0001 of the calibrated data (Figure S1 in Supporting Information S1). Overall, the calibrated data have bias and root-mean-square of the differences of the order 10^{-4}, which is better than the Deep SOLO salinity scale resolution and within the target accuracy of 0.002 for the Deep Argo mission (Roemmich, Alford, et al., 2019). Moreover, all differences to the shipboard CTD below 3,000 dbar are within the target accuracy (Table 3).

Using the second deep cast (5 days later) for the comparisons, bias, and root-mean-square of the differences for all floats are similar to the ones shown in Table 3 (omitted for clarity). The second deep cast is independent as it was not used to optimize the compressibility coefficient and confirm the strength of the calibration applied to the salinity observations. We also repeated the same comparison procedure for all subsequent profiles (taken weeks and months after the shipboard CTDs). In that case, statistics of differences (bias and root-mean-square of the

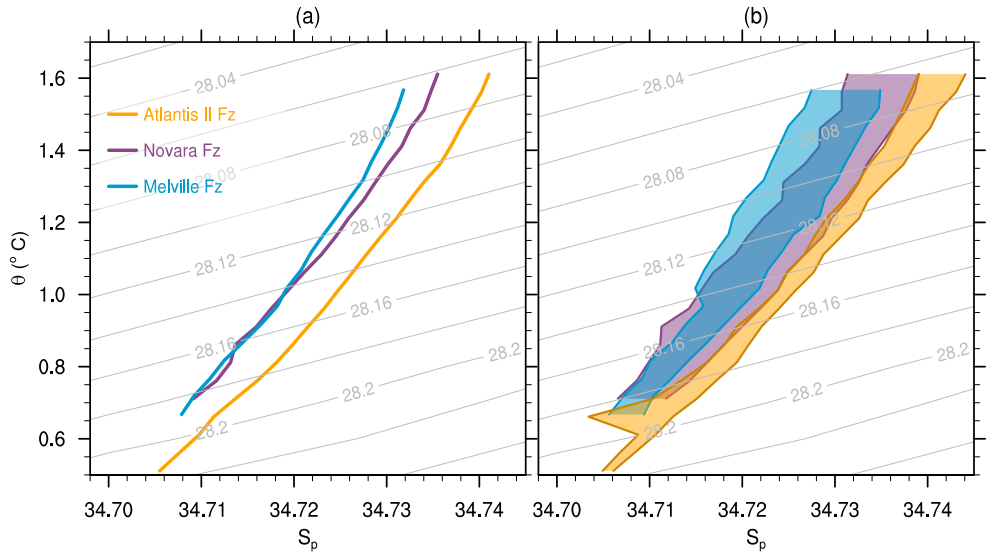

Figure 3. Potential temperature (θ)-practical salinity (S_p) relationships below 3,000 dbar near the Atlantis II, Novara, and Melville fracture zones (Fz): (a) spatiotemporal average and (b) minima/maxima envelope. Statistics were calculated whether three or more data points existed at a given isotherm. Atlantis II Fz data are from 57° to 58°E (16 profiles), Novara Fz from 58° to 59.1°E (16 profiles), and Melville Fz from 60.8° to 61.5°E (20 profiles). Gray curves are neutral densities (γ) in kg/m^3. The color scheme (legend) is the same in (a) and (b).

differences) tend to increase slightly (but still in the same order) as the time in relation to the shipboard CTD increases. These results indicate a robust calibration in salinity and no temporal drift in the conductivity sensor in the first 7 months of operation for any of the three floats.

The Atlantis float is particularly valuable for evaluating temporal drift as the float has primarily stayed in the same area since deployment (Figure 1c). Compared to the accompanying shipboard salinity profile, the root-mean-square of the differences for Atlantis float in the deep ocean (>3,000 dbar) varies from 0.0005 to 0.0023 in the first 32 days and ranges between 0.0013 and 0.0025 afterward. Over the 7 months, the bias has never been above 0.0024. All statistics, even those calculated months after the shipboard CTD acquisition, are within the Deep Argo program target. This short evaluation indicates the quality of the calibrated Deep SOLO salinity observations.

4.2. Mean Temperature-Salinity Relationship

The floats reveal that the abyssal water near the deep fracture zones in the central-eastern Southwest Indian Ridge has distinct temperature and salinity properties. While the mean θ-S_p relationships below 3,000 dbar are dominated by the mixing between the Antarctic Bottom Water and the overlying Circumpolar Deep Water/North Atlantic Deep Water, in the area near the Atlantis II fracture zone, the abyssal water below 3,000 dbar is saltier than near Novara and Melville on average (Figure 3a). The mean θ-S_p curves are offset by about 0.005 in salinity at a given isotherm (Figure 3a), which is above the salinity measurement uncertainty described in the previous section.

The distinction in abyssal water properties is also evident in other statistics. For instance, Figure 3b shows the minimum and maximum salinity envelope on isotherms over areas close to Melville (blue shading) and Atlantis II (orange shading) fracture zones. The envelopes of minima and maxima from these two regions almost do not overlap, and abyssal water denser than $\gamma = 28.06$ kg/m^3 is always fresher and colder on average at a given isopycnal in the Melville region. Like Melville, the Novara area is also fresher than Atlantis II on average (Figure 3a, purple curve). However, when we look at the envelope around the average (Figure 3b, purple shading), we can see some overlap of Novara with Atlantis II and Melville.

The displacement of the mean temperature-salinity curves shown in Figure 3 suggests a salinity gradient along the northern flank of the central-eastern Southwest Indian Ridge, as described in more detail in the following sections. The gradation in temperature-salinity properties is also distinguishable at individual profiles (Figure S4 in

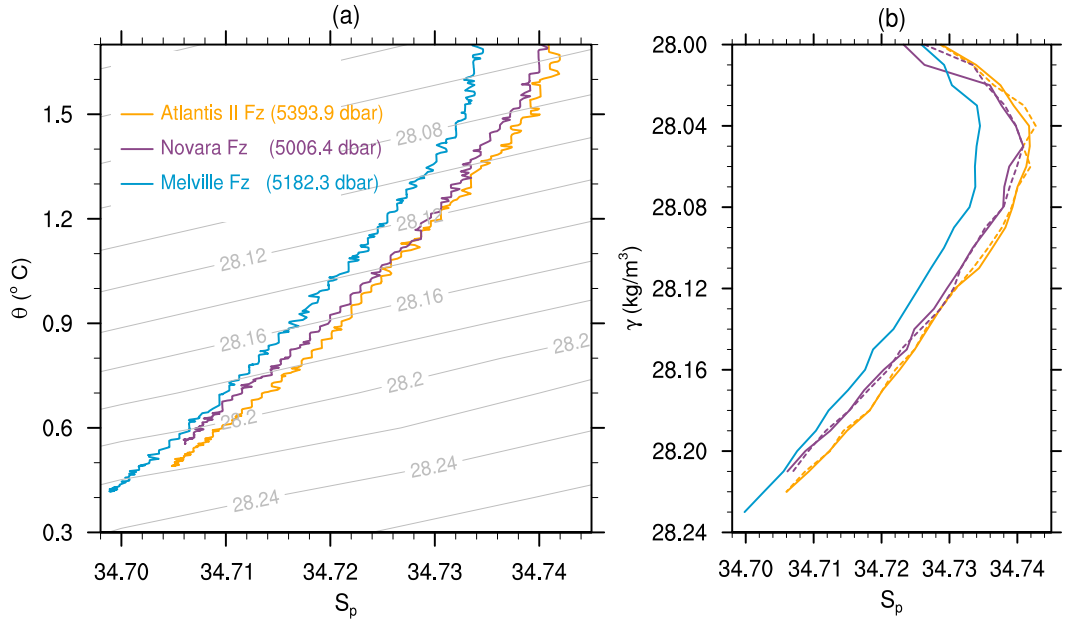

Figure 4. Potential temperature (θ) and practical salinity (S_p) below 3,000 dbar measured at the valleys of Atlantis II, Novara, and Melville fracture zones: (a) θ-S_p relationships of the deepest casts and (b) S_p on neutral densities (γ) for casts reaching below 5,000 dbar. Both panels use the same color scheme (legend) in which values between parenthesis are the maximum pressure sampled at the respective cast. In (a), Atlantis II data was collected at 57.207°E; 29.8°S on 27 December 2023, Novara at 58.013°E; 29.633°E on 24 October 2023, and Melville at 61.038°E; 27.746°S on 28 June 2023. In (b), solid curves show salinity from the same casts as in (a), and dashed curves are the second cast measured at the valleys of Atlantis II (57.254°E; 29.79°S on 27 December 2023; maximum depth of 5,093.7 dbar) and Novara (58.118°E; 29.611°S on 18 October 2023; maximum depth of 5,006 dbar) fracture zones. Wiggles at θ-S_p curves are due to the truncation-related noise in the high-vertical resolution salinity profiles described in Section 3.1.2.

Supporting Information S1). Atlantis II's saltiness and Melville's freshness are also seen in the valleys of these deep fracture zones. Figure 4a shows the θ-S_p relationships below 3,000 dbar there. Distinct from mean θ-S_p, potential temperature is as low as 0.4°C in the cast taken at Melville's valley, capturing a less mixed Antarctic Bottom Water signature.

Although the Atlantis II cast in the fracture zone valley is about 200 dbar deeper than the ones obtained at Melville's valley, the bottom water at the Atlantis II valley is warmer, saltier, and lighter. For the Novara, the θ-S_p curve lies between Atlantis II and Melville for isopycnals $\gamma \geq 28.16$ kg/m^3, which is more on the saltier side of the Novara envelope shown in Figure 3b (purple shading). In density space (Figure 4b), the offset between Atlantis II and Melville is evident, with the latter being fresher by more than 0.03 for all $\gamma \geq 28$ kg/m^3. A second cast reaching below 5,000 dbar in Novara and Atlantis II valleys validate these findings (Figure 4b, dashed curves).

4.3. Spatio-Temporal Temperature-Salinity Distribution and Antarctic Bottom Water Role

Deep Argo floats provide a Lagrangian perspective on the distribution of water mass properties as they move in space and collect data over time. The floats deployed in the Southwest Indian Ridge area show more small-scale variability in abyssal water properties than expected from the limited historical data set and reveal the influence of the Antarctic Bottom Water in setting these patterns. In this section, results are presented separately for each float for the sake of clarity as they have traveled over distinct bottom features. Despite the local differences, below 3,000 dbar, the profiles show a saltier layer over a fresher's bottom. Thus, both temperature and salinity decrease with increasing depth in the fracture zone exit area of the Southwest Indian Ridge.

In the figures of this section, black triangles indicate when the floats touched the actual seafloor, and dashed blue and gray curves show the estimated bottom depths from ETOPO-2022 and GEBCO-2023 data sets. For the Atlantis float, in 50% of the casts, the float touched the actual seafloor, for Novara 49.1%, and Melville 58.2%. There are several instances in which the actual seafloor depth is hundreds of meters above or below the estimated ones (Table 4). Other times, the target depth was shallower than the estimated seafloor (37%–37.7% of the casts),

Table 4
Mean, Minimum, Maximum, and Root-Mean-Square (rmsd) Differences[a] in Meters Between Actual[b] Seafloor Depths[c] and Estimated Depths[c] From ETOPO-2022 and GEBCO-2023 Data Sets

	Mean difference [minimum maximum]		*rmsd*	
Float	ETOPO-2022	GEBCO-2023	ETOPO-2022	GEBCO-2023
Atlantis	57.47 [−261.58 473.46]	29.61 [−323.64 452.96]	201.46	149.26
Novara	−106.73 [−1105.04 430.46]	−91.16 [−1171.43 294.77]	320.16	312.56
Melville	−78.44 [−602.37 167.50]	−90.75 [−821.56 305.03]	206.38	231.43

[a]Differences were computed as the actual seafloor minus the global data sets. Positive values mean the actual seafloor is deeper than the estimated, and negative values mean otherwise. [b]Based on casts in which the float touched the seafloor. [c]The Gibbs-SeaWater Oceanographic toolbox was used to convert from pressure (dbar) to depth (m).

with a mean difference of 398.64 m (ETOPO-2022) and 430.50 m (GEBCO-2023). Moreover, at about 6% of casts, despite the maximum pressure being deeper than the estimated seafloor, the bottom detection system was not triggered (mean difference of 147.92 m for ETOPO-2022 and 120.16 m for GEBCO-2023). These statistics indicate the complexities of navigating over rough terrain.

4.3.1. Melville Float

During the first 7 months of operation, the Melville float traveled between 60.809°–63.093°E and 27.480°–28.118°S in the northeast area of the Southwest Indian Ridge. The float was deployed at the Melville fracture zone valley in May 2023 but displaced northwestward and collected its first deep cast outside the valley. From June to July, the float diagonally crossed the fracture zone in the southeastward direction and obtained its deepest cast on 28 June 2023 (5,182 dbar). Afterward, the float traveled eastward over the wrinkled ridge topography and produced a quasi-zonal section around 27.8°S (Figure 5a). Since September 2023, it entered a relatively shallow area (seafloor above 4,000 m) in its journey to the east. With this trajectory, the float measured different regimes: west and east of the Melville fracture zone, the fracture zone valley, and the ridge.

Colder, fresher, and denser abyssal water is found west of the fracture zone and in the fracture zone valley, with isopycnals greater than $\gamma = 28.18$ kg/m^3 only existing in those regions (Figure 5b, green curves). In addition, a mean east-west gradient is noticeable around the Melville fracture zone below 4,000 dbar. Potential temperature is about 0.1°C colder on the western side on average, and practical salinity is fresher by about 0.01. At the fracture zone valley, which has the coldest and freshest bottom water in the entire section, minimum temperature and salinity are $\theta = 0.417$°C and $S_p = 34.699$, respectively, with a maximum density of $\gamma = 28.233$ kg/m^3 (Figure 4). Over the ridge (seafloor <4,000 dbar), the water near the bottom is warmer (θ = 1–1.2°C), saltier ($S_p \approx 34.73$), and lighter ($\gamma \approx 28.11$) than closer to Melville (Figure 5b).

The stratification of potential temperature is similar throughout the section traced by the Melville float for pressures above 4,000 dbar. However, salinity has a zonal gradient (Figure 5b). Mean practical salinity between 3,000 and 4,000 dbar steadily increases from 34.721 (near the fracture zone) to 34.735 (over the ridge), which is also evident on isopycnal space in the layer $\gamma = 28.02$–28.12 kg/m^3 (not shown). This salinity increase is likely due to the enhanced influence of the saltier North Atlantic Deep Water, which accounts for about 12% of the mixture in the western side of the section and 19% in the eastern in this layer, as indicated by the water mass mixing analysis (Figure 6a).

As expected, the North Atlantic Deep Water influence decreases with depth. The lowest influence is found in the bottom water western of the fracture zone and at the valley, with North Atlantic Deep Water accounting for a minimum of 6% there (Figure 6a).

Below 4,000 dbar, abyssal water is mainly a mixture of Antarctic Bottom Water (19%–40%) and Circumpolar Deep Water (56%–62%), with Antarctic Bottom Water importance increasing downward (Figure 7a). Antarctic Bottom Water contribution is larger to the west of the Melville fracture zone, peaks at the fracture zone valley, and decreases toward the east. These findings confirm that the Melville fracture zone acts as a conduit for Antarctic-originated water to enter the Madagascar Basin and suggests a westward advection of this water (Figure 7a).

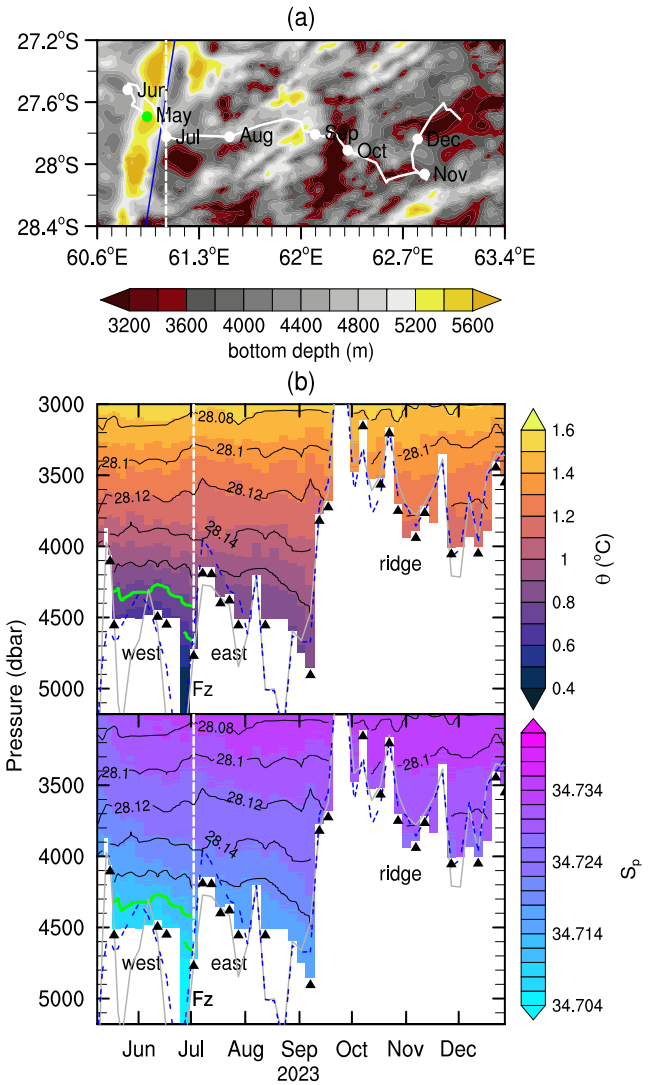

Figure 5. Trajectory, potential temperature (θ), and practical salinity (S_p) data below 3,000 dbar for the Melville float. In (a), bottom topography is from ETOPO-2022, the white line is the float trajectory, the white dots indicate the months the float reached those positions in 2023, and the green dot is the deployment site. A diverging color map is used for plotting the bottom topography, in which yellow highlights the fracture zone valley and dark red the shallowest areas. Blue line marks the Melville central axis from GEBCO Undersea Feature Names Gazetteer. In (b), black contours are neutral densities (γ) in kg/m^3, and the green highlights the densest water ($\gamma \geq 28.18$ kg/m^3). Dashed blue contour shows the estimated seafloor from ETOPO-2022, and the gray is from GEBCO-2023 at the profiles' coordinates. Dashed white lines in (a) and (b) indicate the Melville fracture zone (Fz). Black triangles show casts in which the float touched the seafloor.

4.3.2. Novara Float

The Novara float has explored several areas between 57.207°–59.681°E and 29.456°–30.109°S (Figure 8a), which include the ridge east of the fracture zone (June–September 2023), the valleys of Novara (in May and October) and Atlantis II (December), and the region that lies between these two deep fracture zones (October and November).

In this region of the Southwest Indian Ridge, the water mass decomposition shows a more prominent Antarctic Bottom Water contribution than for the segment sampled by the Melville float (Figure 7b). Similar to Melville, the presence of Antarctic Bottom Water increases downward and reaches a maximum in bottom water, where it accounts for approximately 41% of the mixture. However, Antarctic Bottom Water is also an essential source above 4,000 dbar in the region sampled by the Novara float. For instance, Antarctic Bottom Water's contribution is noteworthy over the relatively shallow ridge east of the Novara fracture zone (data collected over June–September). It accounts for up to 25.5% of the mixture, which is as strong as the contribution of North Atlantic Deep Water (up to 25.3%) in the same layer (Figure 6b). The enhanced Antarctic Bottom Water contribution in the upper abyssal layer suggests vigorous vertical mixing between Novara and Atlantis II fracture zones.

The Novara float was deployed in the fracture zone valley and collected its first cast in the Novara fracture zone on 12 May 2023 (4,504 dbar at 58.817°; 29.456°S). Minimum bottom water temperature and salinity were $\theta = 0.698$°C and $S_p = 34.707$, and maximum density of $\gamma = 28.189$ kg/m^3. Below 4,000 dbar, Antarctic Bottom Water contributes between 31.2% and 35.5% of the mixture and Circumpolar Deep Water to about 49.4%–51.3%. Afterward, the float displaced southeastward and made an anticlockwise loop over the ridge from June to September. The ridge here is overall deeper than near Melville, and the float even encountered an unnamed depression in early July (4,505–4,507 dbar; 59.631°–59.681°E; 29.910°–29.921°S). Bottom water in the depression was colder, denser, and fresher than measured initially at the Novara fracture zone with $\theta = 0.607$°C, $\gamma = 28.203$ kg/m^3 and $S_p = 34.705$, respectively. Antarctic Bottom Water contribution is higher in the depression, up to 37.8%, and Circumpolar Deep Water lower (50.5%). These results show that Antarctic Bottom Water is also present in minor deep bottom topography features.

After sampling the ridge for 4 months, the float drifted westward in a quasi-zonal section around 29.6°S (Figure 8a). This section started at 59.452°E over the ridge, crossed the Novara fracture zone for a second time in October, and reached the Atlantis II fracture zone by the end of November (57.669°E). As the float progressed westward, colder and fresher abyssal water was seen. In the second Novara crossing (which is slightly southward of the first), the casts were deeper (5,006–5,006.4 dbar) than in the first time, and Novara bottom water was found as cold as $\theta = 0.554$°C, fresh as $S_p = 34.705$ and dense as $\gamma = 28.213$ kg/m^3 (Figure 4). Maximum Antarctic Bottom Water contribution was 39.3% and Circumpolar Deep Water 48.1%. At the Atlantis II valley, the cast was even deeper (5,393.9 dbar), and the bottom water has $\theta = 0.491$°C, $S_p = 34.705$, and $\gamma = 28.223$ (Figure 4), with Antarctic Bottom Water accounting for 40.9% of the mixture and Circumpolar Deep Water for 47.2% (Figure 4).

Between Novara and Atlantis II fracture zones, the float observed a shoaling of the deepest isopycnals ($\gamma \geq 28.20$ kg/m^3) corresponding to the increasing presence of the coldest and freshest bottom water, followed by isopycnal deepening when the float moved away (Figure 8b). A thick Antarctic Bottom Water layer is seen in the Novara and Atlantis II valleys and the region separating these two fracture zones (Figure 7b). In summary, the

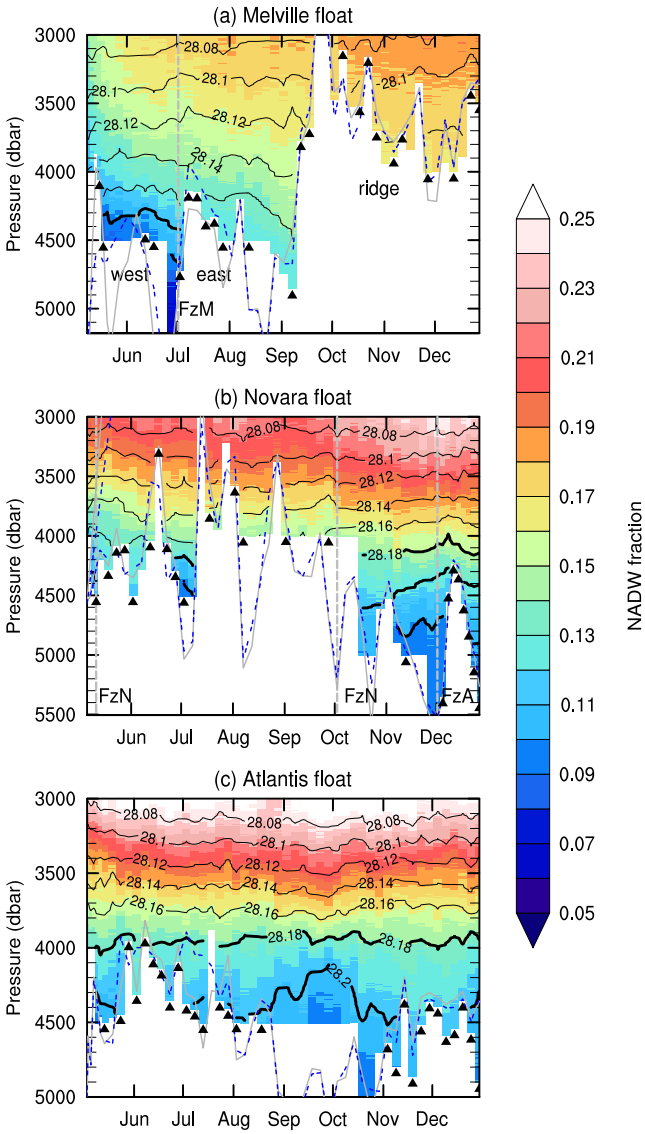

Figure 6. Mean North Atlantic Deep Water contribution for the mixture from the water mass mixing analysis for the data collected by (a) Melville, (b) Novara, and (c) Atlantis floats. Shading is the North Atlantic Deep Water fraction, and black contours are neutral densities (γ) in kg/m^3. Thick black contours highlight isopycnals $\gamma \geq 28.18$ kg/m^3. FzM stands for Melville fracture zone, FzN for Novara fracture zone, and FzA for Atlantis II fracture zone, and dashed gray lines indicate their positions in the data. Dashed blue contour shows the estimated seafloor from ETOPO-2022 at the profiles' coordinates, and the gray is from GEBCO-2023. Black triangles show casts in which the float touched the seafloor.

results presented in this section indicate that Antarctic-originated bottom water is also transported through the Novara fracture zone.

4.3.3. Atlantis Float

Distinct from Melville and Novara floats, the Atlantis float has zonally displaced less than 50 km (56.4°–56.8°E) in the 7 months of operation (Figure 9a). The float was deployed 67.8 km west of the Atlantis II fracture zone within an unnamed deep feature (>5,000 dbar). This deep feature is part of a Southwest Indian Ridge non-transform discontinuity at 56.5°E (Baines et al., 2007), which (current) bathymetric maps do not indicate to be directly connected with the Crozet Basin at the Antarctic Bottom Water layer. Latitudinally, the float has displaced about 70 km (30.4°–31.15°S) more or less parallel to this feature, forming a quasi-meridional section.

After deployment, the float moved southward from May to June 2023 and made an anticlockwise loop near 31.1°S–54.5°E (June and July) before moving northward, west of the deepest area. It arrived at 30.7°S in August, and through a clockwise loop, the float approached the unnamed deep area again but northward of the deployment site. It remained in this area from September to November before drifting northwestward.

Vertical stratification in potential temperature and practical salinity measured by the Atlantis float resemble that measured by Novara and Melville floats in which θ and S_p decrease toward the seafloor everywhere in the section (Figure 9b). During its trajectory, the float encountered the coldest and freshest bottom water between August and November, near the deep unnamed feature at 56.7°–56.8°E. It recorded its deepest casts in this feature by the end of October (5,005 dbar), with bottom water having a potential temperature of 0.551°C, practical salinity of 34.703, and a neutral density of 28.212 kg/m^3. In terms of water mass composition, Antarctic Bottom Water contributed up to 39.2% to the bottom water mixture, whereas Circumpolar Deep Water accounted for 47.4%.

As the float approached the deepest area, the $\gamma = 28.2$ kg/m^3 isopycnal shoaled by about 400 dbar (from 4,500 to 4,000 dbar). It deepened to 4,500 dbar and disappeared as the float moved northwestward (Figure 9b). This vertical movement was only observed in the densest layer ($\gamma \geq 28.2$ kg/m^3; pressure >4,000 dbar). Concurrently with the isopycnal displacement, there was an increase in Antarctic Bottom Water contribution to about 39.4% (Figure 7c). Unfortunately, the entire thickness of the Antarctic Bottom Water-enhanced layer in this area seems not to have been sampled by the float as the target depth was shallower, 500 dbar or more, than the ETOPO-2022 or GEBCO-2023 seafloors, and the float has not touched the bottom (Figure 7c, dashed blue curve). However, as previously discussed, the bottom depths from global data sets are not accurate enough at small scales in this region, making it hard to know what fraction of the bottom layer has not been captured.

Although the deep feature located at 56.8°E seems not to be directly linked to the Crozet Basin, it is filled with bottom water that has similar θ-S_p-γ properties as the bottom water sampled in the Atlantis II, Novara, and Melville valleys. In addition, Antarctic Bottom Water accounts for a comparable fraction of the mixture (Figure 7c). Assuming that no direct connection exists with the Crozet Basin (source of Antarctic Bottom Water to the Madagascar Basin) through this deep feature, we conjecture that bottom water in this deep feature originated from one of the main fracture zones of the Southwest Indian Ridge (Atlantis II, Novara, and Melville). Because these fracture zones are east of the 56.7–56.8°E deep feature, this fact suggests a westward advection of bottom water in this region.

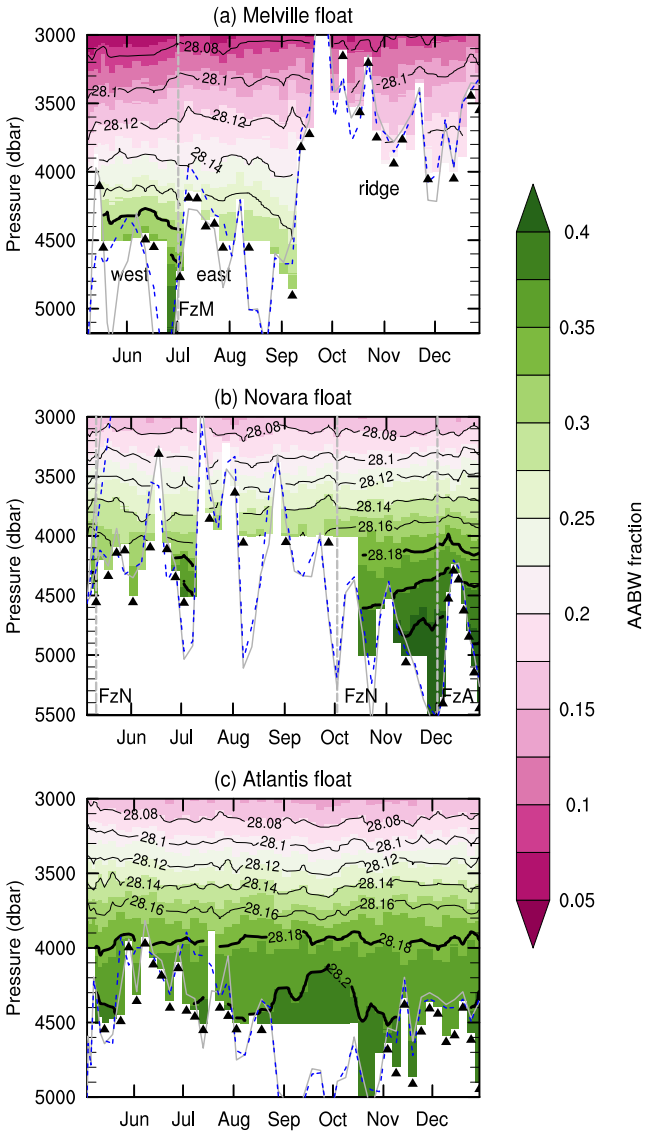

Figure 7. Mean Antarctic Bottom Water contribution for the mixture from the water mass mixing analysis for the data collected by (a) Melville, (b) Novara, and (c) Atlantis floats. Shading is the Antarctic Bottom Water fraction, and black contours are neutral densities (γ) in kg/m^3. Thick black contours highlight isopycnals $\gamma \geq 28.18$ kg/m^3. FzM stands for Melville fracture zone, FzN for Novara fracture zone, and FzA for Atlantis II fracture zone, and dashed gray lines indicate their positions in the data. Dashed blue contour shows the estimated seafloor from ETOPO-2022 at the profiles' coordinates, and the gray is from GEBCO-2023. Black triangles show casts in which the float touched the seafloor.

The Atlantis float data also reveals that Antarctic Bottom Water plays a substantial role in the upper abyssal layer (above 4,000 dbar), with a minimum contribution of 13.6% and a maximum of 36.5% (Figure 7c), which is consistent with the findings from Novara float. Both data sets suggest vigorous vertical mixing in this area of the Southwest Indian Ridge.

4.3.4. Gradients Along the Southwest Indian Ridge and Fingerprints of Antarctic Bottom Water

By comparing the water mass decomposition from the three floats, which cover the fracture zone exit area between 56°E and 63°E, we observe a persistent decrease in the relative contributions of Antarctic Bottom Water and North Atlantic Deep Water to the upper abyssal layer (<4,000 dbar) as we move from the southwest (Atlantis float) to the northeast (Melville float). To illustrate this, Figure 10a shows the Antarctic Bottom Water and North Atlantic Deep Water fractions at $\gamma = 28.1$ kg/m^3 (3,200–3,400 dbar), which is on the core of the upper abyssal layer, as a function of longitude. There is a jump in the relative contributions with a discontinuity between 59.7°E and 60.8°E where no float had sampled. The Antarctic Bottom Water and North Atlantic Deep Water patterns mean that the Circumpolar Deep Water contributes less to the upper abyssal layer in the southwestern and more to the northeast. Despite the reduced North Atlantic Deep Water contribution in the northeast, a persisting increase is observed east of the Melville fracture zone (from 16% to 19%) as previously described.

The reduction in the contribution of North Atlantic Deep Water toward the northeast is also observed for the densest layer ($\gamma \geq 28.2$ kg/m^3) as shown in Figure 10b. This densest layer does not exist over the ridge east of the Melville fracture zone (>61°E) because the ridge is a physical barrier for the Antarctic Bottom Water intrusion in the Madagascar Basin. Over the ridge, the float sampled the entire water column, and most casts touched the actual seafloor (Figure 5, black triangles). The North Atlantic Deep Water decrease suggests that the abyssal water below 3,000 dbar is overall fresher near the Melville fracture zone (Figures 3 and 4) because there is less influence of this saltier water mass in both the upper abyssal and the bottom water there. The fact that the lighter North Atlantic Deep Water contributes 10%–13% to bottom water west of the Novara fracture zone while the denser Antarctic Bottom Water contributes 20%–21% to the upper abyssal layer corroborates the hypothesis of vigorous vertical mixing in this area.

Additionally, the floats reveal a consistent reduction in the Antarctic Bottom Water layer thickness (a depth-integrated quantity) below 3,000 dbar toward the northeast. Between the Atlantis II and Novara fracture zones, the Antarctic Bottom Water layer thickness accounts for up to 34% of the abyssal water column, but east of the Melville fracture zone, it drops to about 20% and further decreases eastward (Figure 11, bottom panel). Besides this large-scale pattern, local peaks in Antarctic Bottom Water layer thickness are observed at the locations of the fracture zones and the deep (unnamed) features previously described. In these regions where Antarctic-originated water enters the Madagascar Basin, the Circumpolar Deep Water and North Atlantic Deep Water layers are thinner (local minimum).

While the Antarctic Bottom Water layer contracts to the northeast, the Circumpolar Deep Water expands (Figure 11, middle). However, a similar large-scale trend is not evident for the North Atlantic Deep Water. In the latter case, the normalized water-class layer thickness mostly oscillates between 15% and 20% west of 60°E, with a positive trend observed east of the Melville fracture zone (Figure 11, top panel).

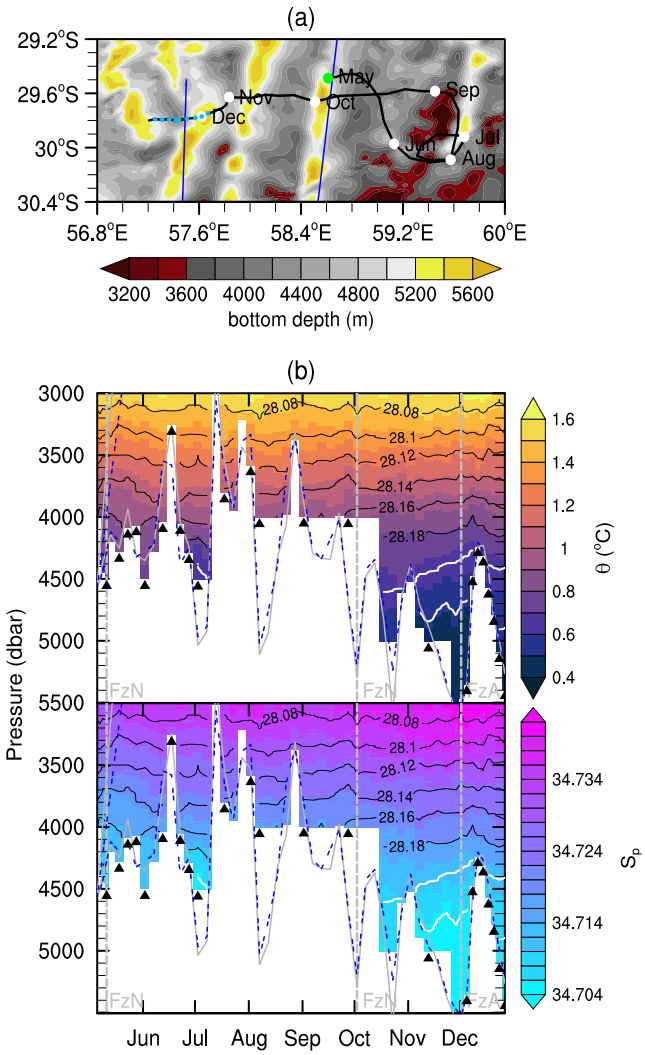

Figure 8. Trajectory, potential temperature (θ), and practical salinity (S_p) data for the Novara float. In (a), shading is the bottom topography, the black line is the float trajectory, large dots indicate the months the float reached those positions in 2023, and the green dot marks the deployment site. Blue lines mark the Atlantis II and Novara central axes from GEBCO Undersea Feature Names Gazetteer. Small cyan dots show the Atlantis II fracture zone area. Bottom topography is from ETOPO-2022 (NCE, 2022) and plotted using a diverging color map (yellow associated with the deepest areas and dark red with the shallowest). In (b), black contours are neutral densities (γ) in kg/m^3, and white contours highlight the densest water ($\gamma \geq 28.20$ kg/m^3). Dashed blue contour shows the estimated seafloor from ETOPO-2022 at the profiles' coordinates, and the gray is from GEBCO-2023. Dashed gray lines indicate Novara (FzN) and Atlantis II (FzA) fracture zone positions, respectively. Black triangles show casts in which the float touched the seafloor.

Discernible zonal patterns along the Southwest Indian Ridge also emerge upon examining the bottom (densest) water at each profile. Generally, bottom water became warmer, saltier, and lighter toward the northeast as the seafloor along the Southwest Indian Ridge northern flank became gradually shallower, with less presence of Antarctic Bottom Water as a consequence (Figure 12). East of the Melville fracture zone, where the seafloor is the shallowest in average (<4,000 m), bottom water is very light ($28.08 < \gamma < 28.14$ kg/m^3, Figure 12a). In this region, the Antarctic Bottom Water layer is relatively thin (Figure 11), and Antarctic Bottom Water contribution is the lowest (Figure 12b). Similarly, lighter ($\gamma < 28.14$ kg/m^3) and warmer bottom water ($\theta \geq 1.2$°C), with lower Antarctic Bottom Water contribution and higher salinity, are also observed when the floats sampled over the relatively shallow ridge between 59.5°E and 60°E.

The exception to the large-scale pattern described above is observed near the fracture zones where Antarctic Bottom Water contribution to bottom water is maximum (Figure 12b, red dots). As described in previous sections, bottom water at Melville exit (northeastern) is colder, fresher, and denser than at Novara and Atlantis II (southwestern) (Figures 12a and 12b–12d, red dots).

Atlantis II, Novara, and Melville fracture zones are deep features of the bottom topography with valleys deeper than 5,000 m. Thus, the abyssal layer (below 3,000 dbar) in these features is thicker than in the shallower surrounding areas. Despite that, the normalized Antarctic Bottom Water layer thickness (which is the equivalent water-class layer thickness divided by the abyssal layer thickness) shown in Figure 11 peaks at the fracture zone exits, further illustrating the strong Antarctic Bottom Water presence in the fracture zones. Moreover, the Antarctic Bottom Water contribution is similar in the three fracture zones (Figure 12b). These facts suggest that Novara and Melville are as important as Atlantis II in steering Antarctic-originated water to the Madagascar Basin.

5. Summary and Discussion

The present study used relatively new technology (Deep SOLO floats) to revisit a 50-year-old puzzle about the Antarctic Bottom Water export to the Madagascar Basin through the deep fracture zones of the Southwest Indian Ridge, particularly the possible Antarctic Bottom Water inflow from the Melville, the most northeastern fracture zone. The Deep SOLO floats implemented during the DMB experiment in May 2023 in only 7 months of operation from their expected 4-year mission have already collected the largest number of high-resolution temperature and salinity profiles in the central-eastern portion of the Southwest Indian Ridge northern flank (56.3°–63.1°E and 27.4°–31.2°S). This unprecedented data set allowed us to investigate the intrusion of the Antarctic Bottom Water in the Madagascar Basin in detail for the first time.

For the present work, we analyzed 151 profiles reaching below 3,000 dbar from the first 7 months of float operation. To date, this data set provides the most comprehensive and consistent view of the Antarctic Bottom Water intrusion in the central-eastern Madagascar Basin. For context, Le Pichon (1960) had only two hydrographic stations near the northern flank of Southwest Indian Ridge, Warren (1974) one station (same from Le Pichon (1960)), Kolla et al. (1976) less than five and Warren (1978) had ten (later used by Swallow and Pollard (1988)). Toole and Warren (1993) and Donohue and Toole (2003) had overall better spatial resolution but lacked stations in the exit of the deep fracture zones, MacKinnon et al. (2008) measurements were limited to the Atlantis II, and Arvapalli et al. (2022) to the rift valley east of 63°E.

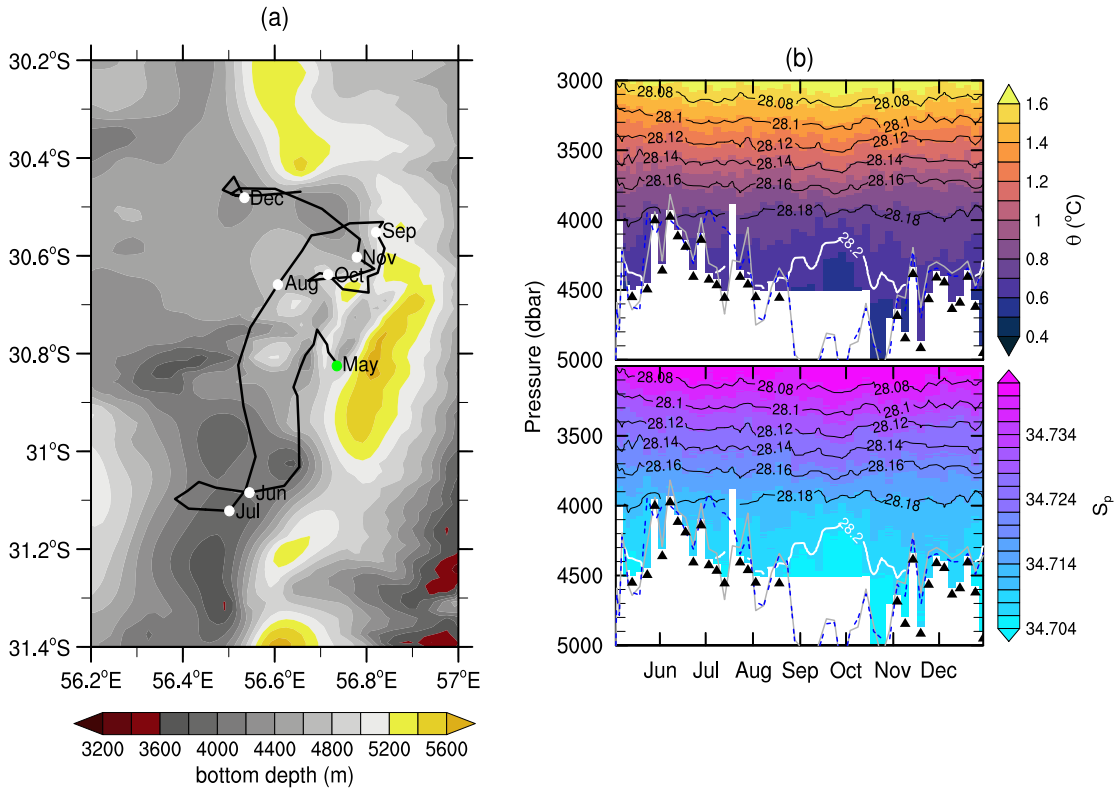

Figure 9. Trajectory, potential temperature (θ), and practical salinity (S_p) data for the Atlantis float. In (a), shading is the bottom topography, the black line is the float trajectory, and the dots indicate the months the float reached its respective positions in 2023. The green dot is the deployment position. Bottom topography is from ETOPO-2022 (NCE, 2022) and plotted using a diverging color map (yellow associated with the deepest areas and dark red with the shallowest). In (b), black contours are neutral densities (γ) in kg/m^3, and white contours highlight the densest water ($\gamma \geq 28.20$ kg/m^3). Dashed blue contour shows the estimated seafloor from ETOPO-2022 at the profiles' coordinates, and the gray is from GEBCO-2023. Black triangles show casts in which the float touched the seafloor.

As of the time of writing, the DMB floats are still operational. If they continue to perform well, we will have numerous additional observations, enabling further studies of Antarctic Bottom Water in the Madagascar Basin. Unlike the regional Deep Argo arrays, in which deep floats are drifting over a relatively flat abyssal plain (e.g.,

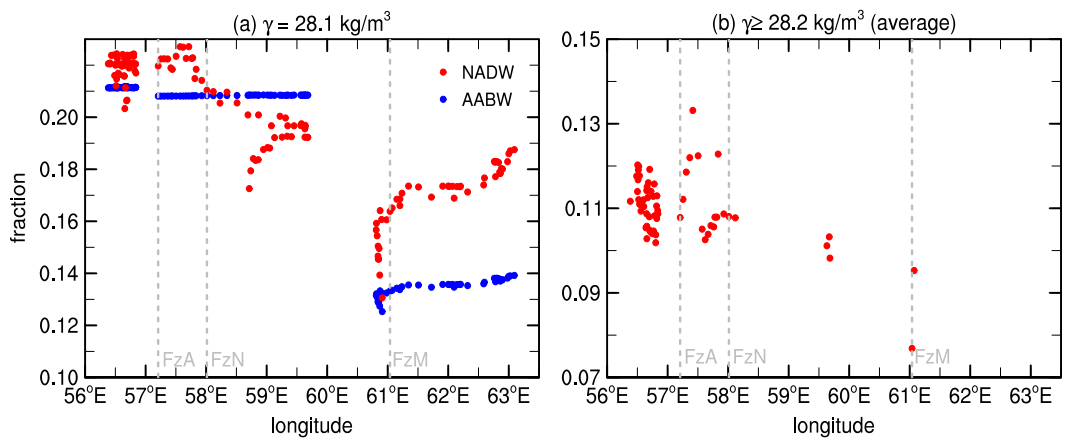

Figure 10. Water mass contribution (fraction) to mixture along the Southwest Indian Ridge as a function of longitude: (a) at $\gamma = 28.10$ kg/m^3 and (b) average for $\gamma \geq 28.2$ kg/m^3. Blue dots represent the Antarctic Bottom Water (AABW), and red dots represent the North Atlantic Deep Water (NADW). In (a), only profiles that reached below 3,000 dbar are shown, and in (b), only those that are denser than $\gamma \geq 28.2$. Dashed gray lines mark data in the valleys of the fracture zones: Atlantis II (FzA), Novara (FzN), and Melville (FzM).

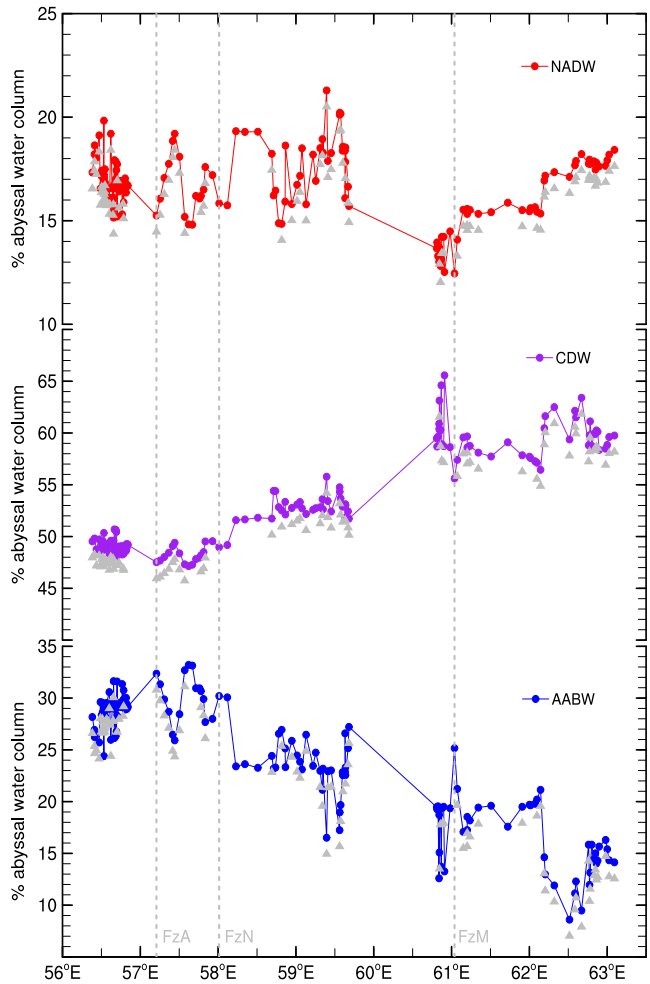

Figure 11. Normalized thickness for North Atlantic Deep Water (NADW; top panel), Circumpolar Deep Water (CDW; mid), and Antarctic Bottom Water (AABW; bottom) as a function of longitude. They express the equivalent water-class layer thicknesses divided by the thickness of the water column below 3,000 dbar (abyssal layer thickness = P_{max} − 3,000). The maximum pressure observed by the float at each profile (P_{max}) has been used as a proxy for the seafloor depth. Only casts that reached below 3,000 dbar are shown. Dashed gray lines indicate the data in the valleys of the fracture zones: Atlantis II (FzA), Novara (FzN), and Melville (FzM). Gray triangles show all casts in which the float touched the seafloor. The overall tendencies are independent of whether the float sampled the whole water column.

Foppert et al., 2021; Johnson, 2022; Johnson & King, 2023; Johnson et al., 2022; Zilberman et al., 2020), we are operating over rough terrain that has not been well-mapped at small scales. Our floats have touched the seafloor many times, which is sometimes well above or below the bottom depths from the most recent global relief data sets. van Wijk et al. (2022) describes a new effort in which information from Argo and Deep Argo floats when grounded is expected to assist in improving the estimation of the global bathymetry in the future.

The comparison with high-quality shipboard observations obtained after each float deployment during the DMB experiment, which have the same accuracy as the gold-standard GO-SHIP measurements (Hood et al., 2010), revealed the calibrated and adjusted salinity measurements from these three floats ($rmsd$ = 0.0007–0.0009 and $bias = 9.3 \times 10^{-6} - 0.0004$) are consistent with the Deep Argo target accuracy (±0.002) (Zilberman et al., 2023). However, we observed a step-like noise with an amplitude of 0.001 in the salinity profiles in the deep ocean (>3,000 dbar) when we increased the vertical resolution to 5-dbar. This noise (only present in salinity) caused excessive density inversions, more than three times those found in high-vertical resolution shipboard profiles or DMB floats collected at 20-dbar resolution in the deep ocean. We traced this issue back to the data compression used in Deep SOLO floats, which gives the salinity scale a resolution of 0.001 and, therefore, does not resolve subtle vertical salinity gradients. We mitigate the noise by slightly adjusting the salinity measurements while

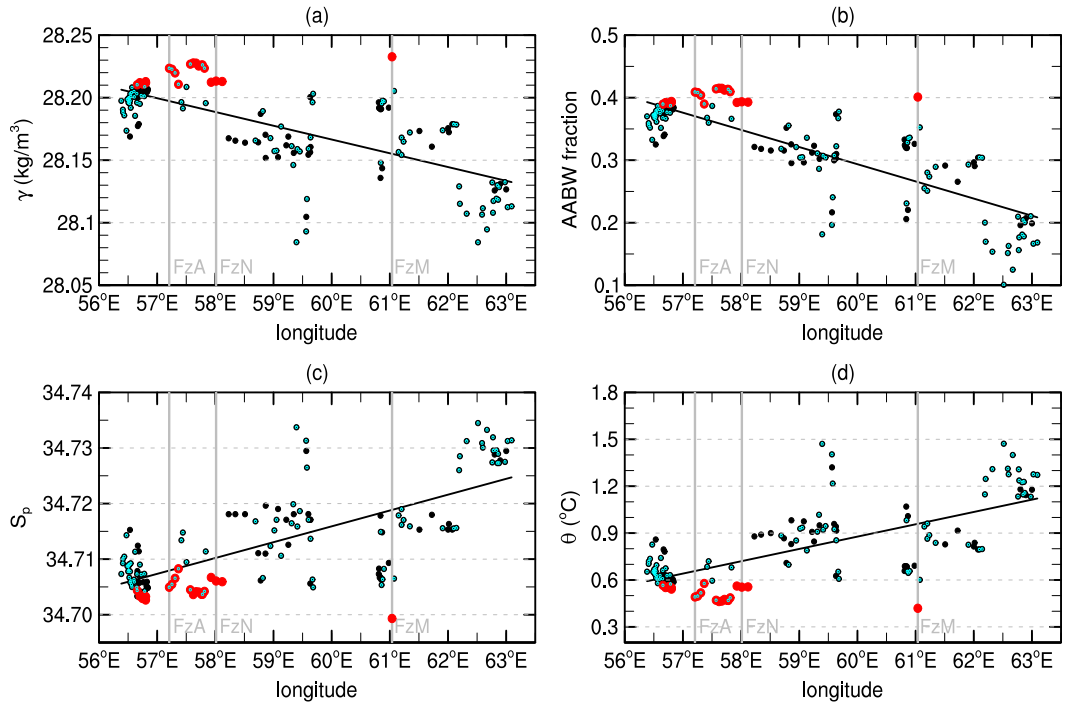

Figure 12. Bottom water properties as a function of longitude: (a) neutral density (γ), (b) Antarctic Bottom Water fraction, (c) practical salinity (S_p), and (d) potential temperature (θ). Red dots highlight the densest water ($\gamma \geq 28.21$ kg/m^3). Gray lines mark the valleys Atlantis II (FzA), Novara (FzN), and Melville (FzM) fracture zones. Cyan dots highlight the casts in which the float touched the seafloor. The overall tendencies are independent of whether the float sampled the actual bottom.

keeping temperature and pressure untouched, following McDougall and Barker (2011). Though this approach reduced the noise substantially, it did not eliminate it, as seen in the temperature-salinity diagram of Figure 4a. Further steps, such as filtering, need to be applied to the salinity profiles from the DMB floats if vertical gradients are required to be calculated.

For this study, we derived optimal compressibility coefficients for the DMB floats to calibrate the salinity measurements as described in Section 3.1.1 and applied them to the original data before investigating the Antarctic Bottom Water intrusion in the Madagascar Basin. However, we wish to emphasize that the data currently available in real-time through the Argo program do not have the optimal coefficient applied yet, as the procedure was carried out offline. We anticipate that this correction will be incorporated soon during the real-time processing.

The DMB floats reveal that the Madagascar Basin abyss has more sources of ventilation in the central-eastern portion than has been described in the literature. Most bottom water studies in this area focused on the contribution of the Atlantis II fracture zone (e.g., Donohue & Toole, 2003; MacKinnon et al., 2008; Toole & Warren, 1993). However, as initially described by Warren (1978), there is Antarctic Bottom Water inflow through the Melville fracture zone, and the DMB floats provide robust evidence of this as described in Section 4.3.1, solving the doubts raised by Toole and Warren (1993). Our float data suggest that the incoming Antarctic Bottom Water through the Melville fracture zone is advected westward since in the region around this fracture zone, bottom water below 4,000 dbar ($\gamma \geq 28.16$ kg/m^3) in the western side exhibits a higher fraction of Antarctic Bottom Water, lower potential temperature and salinity, and higher density than eastern of the fracture zone. The floats also uncovered the Antarctic Bottom Water contribution from the Novara fracture zone (Figures 7b and 8), a contribution that was unknown until the DMB float implementation.

While the Novara fracture zone is well known in the marine geology community (e.g., Baines et al., 2007; Hosford et al., 2003; Patriat et al., 1997, and reference therein), to the best of our knowledge, this fracture zone has not been mentioned in the physical oceanography context even in more recent literature about the deep and abyssal water masses in the region (Donohue & Toole, 2003; Toole & Warren, 1993) despite being more or less

parallel to the Atlantis II, about 130 km east of it and having valley depths of more than 4,500 m. The large number of Antarctic Bottom Water inflows to the Madagascar Basin in the central-eastern portion of the Southwest Indian Ridge is consistent with the results of Cimoli et al. (2023), who show in their Figure 5 that the Madagascar Basin is relatively well-ventilated at the bottom based on analysis of chlorofluorocarbons, at least at the GO-SHIP I07N line at 54.5°E and near the Atlantis II fracture zone at 32°S.

The analysis of the float data reveals that the proportion of Antarctic Bottom Water in the abyssal water is highest near the fracture zones. Specifically, it accounts for up to 41.5% of the bottom mixture at Melville, 39.3% at Novara, and 40.1% at Atlantis II. Therefore, the Antarctic Bottom Water fingerprints are similar in all three deep fracture zones we evaluated. However, a comparison of the volume transport from these fracture zones still needs to be made. According to MacKinnon et al. (2008), an intense northward jet carries 3 Sv of deep and bottom water from the Atlantis II fracture zone. It remains to be seen if Melville and Novara also have similar intense jets in the abyssal ocean and how much water they transport. Evaluating the transports is the next step in our research, as during the DMB experiment, we collected current profiles in high spatial resolution sections within and outside the fracture zones.

Compared with the only two previous measurements, we found bottom water near the Melville fracture zone warmer than in 1976 (Warren, 1978) and colder than in 1960 (Le Pichon, 1960). While the coldest bottom water sampled by the Melville float has in situ temperature of 0.846°C and $\theta = 0.417$°C (61.038°E; 27.746°S), Warren (1978) described the Melville bottom water in 1976 with minimum in situ temperature of 0.78°C and $\theta = 0.3$°C. More than a decade earlier, Le Pichon (1960) reported a station near the Melville fracture zone (although this fracture zone was unknown then) with an in situ temperature of 0.89°C. We limit our discussion here to temperature comparisons only as the historical salinity from Warren (1978) and Le Pichon (1960) would need to be brought to modern standards (Mantyla, 1994), which is outside the scope of the present paper.

The differences in bottom temperature may be related to long-term variability in bottom water properties (e.g., Choi & Nam, 2022; Kouketsu et al., 2011; Menezes et al., 2017; Purkey & Johnson, 2010, 2013; Rhein et al., 2013) and/or distinct vertical/lateral mixing histories as the observations are not exactly from the same positions. The floats have shown much more small-scale spatial variability in the bottom water on the northern flank of the Southwest Indian Ridge than anticipated from previous studies. An investigation of the bottom water temporal variability in the Madagascar Basin is still to be done. Global studies indicate that the Madagascar Basin could have cooled in the last few decades (Kouketsu et al., 2011; Purkey & Johnson, 2010; Rhein et al., 2013), but uncertainty around the trend is too large and not statistically significant.

We find the abyssal water at Melville is fresher and slightly colder than at the Atlantis II fracture zone (Figures 3 and 4). Warren (1978) also described the bottom water properties near the Atlantis II as warmer and saltier than near Melville, but there were only two stations in his study. Here, we show this pattern is robust, with multiple profiles in those regions confirming it. At the Novara valley, bottom water has intermediate temperature-salinity characteristics (Figure 4). These differences are likely due to a distinct history of vertical mixing with the North Atlantic Deep Water, as suggested by the water mass mixing analysis. The North Atlantic Deep Water contribution is larger in the bottom water mixture in the southwestern side of the area sampled by the DMB floats and lower in the northeastern, consistent with van Aken et al. (2004). The latter study shows that along 34°S, the North Atlantic Deep Water has a high salinity core near the Madagascar Plateau, decreasing eastward. However, it is also possible that these deep fracture zones receive inflows from different Antarctic Bottom Water sources around Antarctica, which have distinct temperature-salinity properties (Gordon, 2019; Ohshima et al., 2013, 2022; Orsi et al., 1999). For instance, modeling simulations by Solodoch et al. (2022) suggest that the Antarctic Bottom Water entering the western Indian Ocean is supplied by both the Weddell Sea and Cape Darnley/Prydz Bay varieties. This is a subject for future investigations.

Moreover, the DMB float observations suggest a more vigorous vertical mixing in the southwestern side of our study area, where Antarctic Bottom Water accounts for a significant fraction of the mixture in the upper abyssal layer (3,000–4,000 dbar). This description is consistent with the works of MacKinnon et al. (2008), which measured elevated mixing at the Atlantis II fracture zone, and Huussen et al. (2012) that showed the Southwest Indian Ridge region east of 60°E is a mixing hot spot (their Figure 7).

Apart from the deep fracture zones exit area, where Antarctic Bottom Water has robust fingerprints, the overall bottom water tends to get lighter, warmer, and more saline toward the northeast as the average bottom depths

become shallower. Because there is more Antarctic Bottom Water contribution for the entire water column below 3,000 dbar on the western side than on the eastern, the equivalent thickness of the Antarctic Bottom Water layer (an integrated quantity) also decreases toward the northeast. A similar density pattern was observed by Warren (1978), who suggested that the resulting density gradient would imply a northwestward movement of the deepest layer relative to the above. However, that study lacked the data to investigate further at that time. With the direct observations of currents collected during the DMB experiment, we are starting to explore the bottom circulation near the Southwest Indian Ridge.

Data Availability Statement

DMB Deep SOLO data are available in near real-time through the Argo program repositories and at https://argo.whoi.edu/solo2/12046/index.html (Atlantis float), https://argo.whoi.edu/solo2/12047/index.html (Novara float) and https://argo.whoi.edu/solo2/12048/index.html (Melville float). The software used for the CPcor optimal estimation is available at the Euro-Argo GitHub repository at https://github.com/ArgoDMQC/Deep_Argo_DMTools. The DMB CTD data used for salinity calibration are available at Zenodo data repository (Menezes, 2024), ETOPO-2022 at NOAA National Centers for Environmental Information (NCE, 2022), GEBCO-2023 at https://www.gebco.net/data_and_products/gridded_bathymetry_data/. The Gibbs-SeaWater (GSW) Oceanographic toolbox is available at https://www.teos-10.org/software.htm.

Acknowledgments

We would like to thank the two reviewers and the associate editor for all the suggestions made to improve the manuscript's readability. We extend our sincere appreciation to the hardworking crew of the R/V Roger Revelle, as well as to Captain Dave Murline, for their tireless efforts during the implementation of the DMB Experiment. We would also like to thank the WHOI Argo team for DMB Deep SOLO floats management and the Scripps Ocean Data Facility (ODF) team for the DMB CTD data collection and processing of the data to GO-SHIP standards. We are immensely grateful to the 11 students who participated in the DMB experiment and provided invaluable assistance with CTD collection and float deployment. We would also like to acknowledge the use of the NCL program (https://doi.org/10.5065/D6WD3XH5) for analysis and graphics in this paper. Last but not least, we thank the National Science Foundation (NSF) for supporting this research through Grants OCE-1924431 and OCE-1924388.

References

Amante, C., & Eakins, B. W. (2009). ETOPO1 1 arc-minute global relief model: Procedures, data sources and analysis [Computer software manual]. *NOAA Technical Memorandum NESDIS NGDC-24. National Geophysical Data Center, NOAA*. https://doi.org/10.7289/V5C8276M

Arvapalli, S. R., Bajish, C., & Kurian, P. J. (2022). Hydrographic observations in the rift valley of Southwest Indian Ridge from 63°E–69°E. *Dynamics of Atmospheres and Oceans*, *97*, 101284. https://doi.org/10.1016/j.dynatmoce.2022.101284

Baines, A. G., Cheadle, M. J., Dick, H. J. B., Scheirer, A. H., John, B. E., Kusznir, N. J., & Matsumoto, T. (2007). Evolution of the Southwest Indian Ridge from 55°45é to 62°e: Changes in plate-boundary geometry since 26 Ma. *Geochemistry, Geophysics, Geosystems*, *8*(6), Q06022. https://doi.org/10.1029/2006GC001559

Barker, P. M., & McDougall, T. J. (2017). Stabilizing hydrographic profiles with minimal change to the water masses. *Journal of Atmospheric and Oceanic Technology*, *34*(9), 1935–1945. https://doi.org/10.1175/JTECH-D-16-0111.1

Choi, Y., & Nam, S. H. (2022). East-west contrasting changes in southern Indian Ocean Antarctic Bottom Water salinity over three decades. *Scientific Reports*, *12*(1), 12175. https://doi.org/10.1038/s41598-022-16331-y

Cimoli, L., Gebbie, G., Purkey, S. G., & Smethie, W. M. (2023). Annually resolved propagation of CFCs and SF6 in the global ocean over eight decades. *Journal of Geophysical Research: Oceans*, *128*(3), e2022JC019337. https://doi.org/10.1029/2022JC019337

Desbruyéres, D. G., Bravo, E. P., Thierry, V., Mercier, H., Lherminier, P., Cabanes, C., et al. (2022). Warming-to-cooling reversal of overflow-derived water masses in the Irminger Sea during 2002-2021. *Geophysical Research Letters*, *49*(10), e2022GL098057. https://doi.org/10.1029/2022GL098057

Donohue, K. A., & Toole, J. M. (2003). A near-synoptic survey of the southwest Indian Ocean. *Deep-Sea Research II*, *50*(12–13), 1893–1931. https://doi.org/10.1016/S0967-0645(03)00039-0

Foppert, A., Rintoul, S. R., Purkey, S. G., Zilberman, N., Kobayashi, T., Sallée, B., & Wallace, L. O. (2021). Deep argo reveals bottom water properties and pathways in the Australian-Antarctic basin. *Journal of Geophysical Research: Oceans*, *126*(12), e2021JC017935. https://doi.org/10.1029/2021JC017935

Ganachaud, A., Wunsch, C., Marotzke, J., & Toole, J. (2000). Meridional overturning and large-scale circulation of the Indian Ocean. *Journal of Geophysical Research*, *105*(C11), 26117–26134. https://doi.org/10.1029/2000JC900122

Gao, Z., Chen, Z., Huang, X., Xu, Z., Yang, H., Zhao, Z., et al. (2021). Internal wave imprints on temperature fluctuations as revealed by rapid-sampling deep profiling floats. *Journal of Geophysical Research: Oceans*, *126*(12), e2021JC017878. https://doi.org/10.1029/2021JC017878

Gebbie, G., & Huybers, P. (2010). Total matrix intercomparison: A method for determining the geometry of water-mass pathways. *Journal of Physical Oceanography*, *40*(8), 1710–1728. https://doi.org/10.1175/2010JPO4272.1

GEBCO Compilation Group. (2023). GEBCO 2023 grid [Computer software manual]. https://doi.org/10.5285/f98b053b-0cbc-6c23-e053-6c86abc0af7b

Gordon, A. L. (2019). Bottom water formation. In *Encyclopedia of ocean Sciences* (3rd ed., pp. 120–126). https://doi.org/10.1016/B978-0-12-409548-9.04019-7

Haine, T. W. N., Watson, A. J., Liddicoat, M. I., & Dickson, R. R. (1998). The flow of Antarctic Bottom Water to the southwest Indian Ocean estimated using CFCs. *Journal of Geophysical Research*, *103*(C12), 27637–27653. https://doi.org/10.1029/98JC02476

Hood, E., Sabine, C., & Sloyan, B. M. (2010). In *The GO-SHIP Repeat Hydrography manual: A collection of expert reports and guidelines* (Tech. Rep.). IOCCP Report Number 14. ICPO Publication Series Number 134 Retrieved from http://www.go-ship.org/HydroMan.html

Hosford, A., Tivey, M., Matsumoto, T., Dick, H., Schouten, H., & Kinoshita, H. (2003). Crustal magnetization and accretion at the Southwest Indian Ridge near the Atlantis II fracture zone, 0-25 Ma. *Journal of Geophysical Research*, *108*(B3), 2169. https://doi.org/10.1029/2001JB000604

Huussen, T. N., Naveira-Garabato, A. C., Bryden, H. L., & McDonagh, E. L. (2012). Is the deep Indian Ocean MOC sustained by breaking internal waves? *Journal of Geophysical Research*, *117*(C8), C08024. https://doi.org/10.1029/2012JC008236

IOC, SCOR, & IAPSO. (2010). The international thermodynamic equation of seawater—2010: Calculation and use of thermodynamic properties [Computer software manual]. 196. Retrieved from https://www.teos-10.org/pubs/TEOS-10_Manual.pdf

Jackett, D. R., & McDougall, T. J. (1997). A neutral density variable for the world's oceans. *Journal of Physical Oceanography*, *27*(2), 237–263. https://doi.org/10.1175/1520-0485(1997)027⟨0237:ANDVFT⟩2.0.CO;2

Johnson, G. C. (2008). Quantifying Antarctic bottom water and North Atlantic deep water volumes. *Journal of Geophysical Research*, *113*(C5), C05027. https://doi.org/10.1029/2007JC004477

Johnson, G. C. (2022). Antarctic Bottom Water warming and circulation slowdown in the Argentine Basin from analyses of Deep Argo and historical shipboard temperature data. *Geophysical Research Letters*, *49*(18), e2022GL100526. https://doi.org/10.1029/2022GL100526

Johnson, G. C., & King, B. A. (2023). Zapiola Gyre, velocities and mixing, new Argo insights. *Journal of Geophysical Research: Oceans*, *128*(6), e2023JC019893. https://doi.org/10.1029/2023JC019893

Johnson, G. C., & Lyman, J. M. (2014). Oceanography: Where's the heat? *Nature Climate Change*, *4*(11), 956–957. https://doi.org/10.1038/nclimate2409

Johnson, G. C., Lyman, J. M., & Purkey, S. G. (2015). Informing Deep Argo array design using argo and full-depth hydrographic section data. *Journal of Atmospheric and Oceanic Technology*, *32*(11), 2187–2198. https://doi.org/10.1175/JTECH-D-15-0139.1

Johnson, G. C., Purkey, S. G., & Bullister, J. L. (2008). Warming and freshening in the abyssal southeastern Indian Ocean. *Journal of Climate*, *21*(20), 5351–5363. https://doi.org/10.1175/2008JCLI2384.1

Johnson, G. C., Purkey, S. G., Zilberman, N. V., & Roemmich, D. (2019). Deep Argo quantifies bottom water warming rates in the southwest Pacific Basin. *Geophysical Research Letters*, *46*(5), 2662–2669. https://doi.org/10.1029/2018GL081685

Johnson, G. C., Whalen, C. B., Purkey, S. G., & Zilberman, N. (2022). Serendipitous internal wave signals in Deep Argo data. *Geophysical Research Letters*, *49*(7), e2022GL097900. https://doi.org/10.1029/2022GL097900

Katsumata, K., Purkey, S. G., Cowley, R., Sloyan, B. M., Diggs, S. C., Moore, T. S., et al. (2022). GO-SHIP Easy Ocean: Gridded ship-based hydrographic section of temperature, salinity, and dissolved oxygen. *Scientific Data*, *9*(1), 103. https://doi.org/10.1038/s41597-022-01212-w

King, B., Thierry, V., Zilberman, N., & Walicka, K. (2021). 3rd deep-argo workshop—Workshop report (Tech. Rep.). Retrieved from https://www.euro-argo.eu/content/download/159856/file/DeepArgoWorkshop2021-Report.pdf

Kobayashi, T. (2021). Salinity bias with negative pressure dependency caused by anisotropic deformation of CTD measuring cell under pressure examined with a dual-cylinder cell model. *Deep-Sea Research I*, *167*, 103420. https://doi.org/10.1016/j.dsr.2020.103420

Kobayashi, T., Sato, K., & King, B. A. (2021). Observed features of salinity bias with negative pressure dependency for measurements by SBE 41CP and SBE 61 CTD sensors on deep profiling floats. *Progress in Oceanography*, *198*, 102686. https://doi.org/10.1016/j.pocean.2021.102686

Kolla, V., Sullivan, L., Streeter, S. S., & Langseth, M. G. (1976). Spreading of Antarctic Bottom Water and its effects on the floor of the Indian Ocean inferred from bottom-water potential temperature, turbidity, and sea-floor photography. *Marine Geology*, *21*(3), 171–189. https://doi.org/10.1016/0025-3227(76)90058-X

Kouketsu, S., Doi, T., Kawano, T., Masuda, S., Sugiura, N., Sasaki, Y., et al. (2011). Deep ocean heat content changes estimated from observation and reanalysis product and their influence on sea level change. *Journal of Geophysical Research*, *116*(C3), C03012. https://doi.org/10.1029/2010JC006464

Le Pichon, X. (1960). The deep water circulation in the southwest Indian Ocean. *Journal of Geophysical Research*, *65*(12), 4061–4074. https://doi.org/10.1029/JZ065i012p04061

MacKinnon, J. A., Johnston, T. M., & Pinkel, R. (2008). Strong transport and mixing of deep water through the Southwest Indian Ridge. *Nature Geoscience*, *1*(11), 755–758. https://doi.org/10.1038/ngeo340

Mantyla, A. W. (1994). The treatment of inconsistencies in Atlantic deep water salinity data. *Deep-Sea Research A*, *41*(9), 1387–1405. https://doi.org/10.1016/0967-0637(94)90104-X

Mantyla, A. W., & Reid, J. L. (1995). On the origins of deep and bottom waters of the Indian Ocean. *Journal of Geophysical Research*, *100*(C2), 2417–2439. https://doi.org/10.1029/94JC02564

McCave, I. N., Kiefer, T., Thornalley, D. J. R., & Elderfield, H. (2005). Deep flow in the Madagascar-Mascarene Basin over the last 150000 years. *Philosophical Transactions of the Royal Society A*, *363*(1826), 81–99. https://doi.org/10.1098/rsta.2004.1480

McDougall, T. J., & Barker, P. M. (2011). Getting started with TEOS-10 and the Gibbs seawater (GSW) oceanographic toolbox (p. 28). SCOR/IAPSO WG127.

McDougall, T. J., Jackett, D. R., Millero, F. J., Pawlowicz, R., & Barker, P. M. (2012). A global algorithm for estimating absolute salinity. *Ocean Science*, *8*(6), 1117–1128. https://doi.org/10.5194/os-8-1117-2012

Menezes, V. V. (2024). Deep Madagascar basin (DMB) experiment CTD data for deep SOLO salinity calibration [Dataset]. *Zenodo*. https://doi.org/10.5281/zenodo.10897736

Menezes, V. V., Macdonald, A. M., & Schatzman, C. (2017). Accelerated freshening of Antarctic bottom water over the last decade in the southern Indian ocean. *Science Advances*, *3*(1), e1601426. https://doi.org/10.1126/sciadv.1601426

Murphy, D. J., & Martini, K. I. (2018). Determination of conductivity cell compressibility for Argo program CTDs and MicroCATs. In *2018 ocean sciences meeting*. Retrieved from https://agu.confex.com/agu/os18/meetingapp.cgi/Paper/320883

NCE. (2022). ETOPO 2022 15 arc-second global relief model (bedrock elevation netCDF) [Dataset]. *NOAA National Centers for Environmental Information*. https://doi.org/10.25921/fd45-gt74

NGDC. (2006). National geophysical data center. 2-minute gridded global relief data (ETOPO2) v2 [Dataset]. *National Geophysical Data Center, NOAA*. https://doi.org/10.7289/V5J1012Q

Ohshima, K., Fukamachi, Y., Ito, M., Nakata, K., Simizu, D., Ono, K., et al. (2022). Dominant frazil ice production in the Cape Darnley polynya leading to Antarctic Bottom Water formation. *Science Advances*, *8*(42), eadc9174. https://doi.org/10.1126/sciadv.adc9174

Ohshima, K., Fukamachi, Y., Williams, G. D., Nihashi, S., Roquet, F., Kitade, Y., et al. (2013). Antarctic Bottom Water production by intense sea-ice formation in the Cape Darnley polynya. *Nature Geoscience*, *6*(3), 235–240. https://doi.org/10.1038/ngeo1738

Orsi, A. H., Johnson, G. C., & Bullister, J. L. (1999). Circulation, mixing, and production of Antarctic bottom water. *Progress in Oceanography*, *43*(1), 55–109. https://doi.org/10.1016/S0079-6611(99)00004-X

Owens, W. B., Zilberman, N., Johnson, K. S., Claustre, H., Scanderbeg, M., Wijffels, S., & Suga, T. (2022). Oneargo: A new paradigm for observing the global ocean. *Marine Technology Society Journal*, *56*(3), 84–90. https://doi.org/10.4031/MTSJ.56.3.8

Pardo, P. C., Pérez, F. F., Velo, A., & Gilcoto, M. (2012). Water masses distribution in the Southern Ocean: Improvement of an extended OMP (eOMP) analysis. *Progress in Oceanography*, *103*, 92–105. https://doi.org/10.1016/j.pocean.2012.06.002

Park, H., Gamberoni, L., & Charriaud, E. (1993). Frontal structure, water masses, and circulation in the Crozet Basin. *Journal of Geophysical Research*, *98*(C7), 12361–12385. https://doi.org/10.1029/93JC00938

Patriat, P., Sauter, D., Munschy, M., & Lindsay Parson, L. (1997). A survey of the Southwest Indian Ridge axis between Atlantis II fracture zone and the Indian Ocean triple junction: Regional setting and large scale segmentation. *Marine Geophysical Researches*, *19*(6), 457–480. https://doi.org/10.1023/A:1004312623534

Purkey, S. G., & Johnson, G. C. (2010). Warming of global abyssal and deep Southern Ocean Waters between the 1990s and 2000s: Contributions to global heat and sea level rise budgets. *Journal of Climate*, *23*, 6336–6351. https://doi.org/10.1175/2010JCLI3682.1

Purkey, S. G., & Johnson, G. C. (2013). Antarctic Bottom Water warming and freshening: Contributions to sea level rise, ocean freshwater budgets, and global heat gain. *Journal of Climate*, *26*(16), 6105–6122. https://doi.org/10.1175/JCLI-D-12-00834.1

Rhein, M., Rintoul, S. R., Aoki, S., Campos, E., Chambers, D., Feely, R. A., et al. (2013). Observations: Ocean. In T. F. Stocker & D. Qin (Eds.), *Climate Change 2013: The Physical Science Basis. Contribution of Working Group I to the Fifth Assessment Report of the Intergovernmental Panel on Climate Change* (pp. 255–315).

Rintoul, S. R., Hughes, C., & Olbers, D. (2001). The Antarctic circumpolar current system. In G. Siedler, J. Church, & J. Gould (Eds.), *Ocean circulation and climate*, *International Geophysics* (Vol. 77, pp. 271–302). Academic Press. https://doi.org/10.1016/S0074-6142(01)80124-8

Roemmich, D., Alford, M. H., Claustre, H., Johnson, K., King, B., Moum, J., et al. (2019). On the future of argo: A global, full-depth, multi-disciplinary array. *Frontiers in Marine Science*, *6*, 439. https://doi.org/10.3389/fmars.2019.00439

Roemmich, D., Sherman, J. T., Davis, R. E., Grindley, K., McClune, M., Parker, C. J., et al. (2019). Deep SOLO: A full-depth profiling float for the argo program. *Journal of Atmospheric and Oceanic Technology*, *36*(10), 1967–1981. https://doi.org/10.1175/JTECH-D-19-0066.1

SBE. (2013). AN10-compressibility compensation of Sea-Bird conductivity sensors (Tech. Rep.). In *Sea-bird electronics*. Retrieved from https://www.seabird.com/application-notes

SBE. (2022). SBE 61 deep argo CTDs (Tech. Rep.). In *Sea-bird electronics*. Retrieved from https://www.seabird.com/sbe-61-deep-argo-ctd/product-downloads?id=54627925789

Siegelman, L., Roquet, F., Mensah, V., Riviére, P., Pauthenet, E., Picard, B., & Guinet, C. (2019). Correction and accuracy of high- and low-resolution CTD data from animal-borne instruments. *Journal of Atmospheric and Oceanic Technology*, *36*(5), 745–760. https://doi.org/10.1175/JTECH-D-18-0170.1

Silvano, A., Purkey, S., Gordon, A. L., Castagno, P., Stewart, A. L., Rintoul, S. R., et al. (2023). Observing Antarctic bottom water in the Southern Ocean. *Frontiers in Marine Science*, *10*, 1221701. https://doi.org/10.3389/fmars.2023.1221701

Solodoch, A., Stewart, A. L., Hogg, A. M., Morrison, A. K., Kiss, A. E., Thompson, A. F., et al. (2022). How does Antarctic bottom water cross the Southern Ocean? *Geophysical Research Letters*, *49*(7), e2021GL097211. https://doi.org/10.1029/2021GL097211

Swallow, J. C., & Pollard, R. T. (1988). Flow of bottom water through the Madagascar Basin. *Deep-Sea Research A*, *35*(8), 1437–1440. https://doi.org/10.1016/0198-0149(88)90095-7

Talley, L. D. (2013). Closure of the global overturning circulation through the Indian, Pacific, and Southern oceans: Schematics and transports. *Oceanography*, *26*(1), 80–97. https://doi.org/10.5670/oceanog.2013.07

Talley, L. D., Feely, R. A., Sloyan, B. M., Wanninkhof, R., Baringer, M. O., Bullister, J. L., et al. (2016). Changes in ocean heat, carbon content, and ventilation: A review of the first decade of GO-SHIP global repeat hydrography. *Annual Review of Marine Science*, *8*(1), 185–215. https://doi.org/10.1146/annurev-marine-052915-100829

Tamsitt, V., Talley, L. D., & Mazloff, M. R. (2019). A deep eastern boundary current carrying Indian Deep Water south of Australia. *Journal of Geophysical Research: Oceans*, *124*(3), 2218–2238. https://doi.org/10.1029/2018JC014569

Thomas, G., Purkey, S. G., Roemmich, D., Foppert, A., & Rintoul, S. R. (2020). Spatial variability of Antarctic bottom water in the Australian Antarctic basin from 2018-2020 captured by deep argo. *Geophysical Research Letters*, *47*(23), e2020GL089467. https://doi.org/10.1029/2020GL089467

Tomczak, M., & Large, D. G. B. (1989). Optimum multiparameter analysis of mixing in the thermocline of the eastern Indian Ocean. *Journal of Geophysical Research*, *94*(C11), 16141–16149. https://doi.org/10.1029/JC094iC11p16141

Toole, J. M., & Warren, B. A. (1993). A hydrographic section across the subtropical South Indian Ocean. *Deep-Sea Research I*, *40*(10), 1973–2019. https://doi.org/10.1016/0967-0637(93)90042-2

van Aken, H. M., Ridderinkhof, H., & de Ruijter, W. P. M. (2004). North Atlantic deep water in the south-western Indian Ocean. *Deep-Sea Research I*, *51*(6), 755–776. https://doi.org/10.1016/j.dsr.2004.01.008

van Sebille, E., Spence, P., Mazloff, M. R., England, M. H., Rintoul, S. R., & Saenko, O. A. (2013). Abyssal connections of Antarctic bottom water in a Southern Ocean state estimate. *Geophysical Research Letters*, *40*(10), 2177–2182. https://doi.org/10.1002/grl.50483

van Wijk, E. M., Hally, B., Wallace, L. O., Zilberman, N., & Scanderbeg, M. (2022). Can Argo floats help improve bathymetry? *International Hydrographic Review*, *28*, 226–230. https://doi.org/10.58440/ihr-28-n08

Walicka, K., King, B., Cabanes, C., Thierry, V., Desbruyeres, D., Gilson, J., et al. (2020). D3.2: Design of a comparative study on DMQC methods used for deep argo (Tech. Rep.). *Zenodo*. https://doi.org/10.5281/zenodo.4561757

Walicka, K., King, B., Thierry, V., Cabanes, C., Vélez-Belchí, C. C. P., Notarstefano, G., et al. (2022). D3.4: Report of the outcome of the comparative study for the deep Argo quality control processing (Tech. Rep.). *Zenodo*. https://doi.org/10.5281/zenodo.8366454

Warren, B. A. (1974). Deep flow in the Madagascar and Mascarene basins. *Deep-Sea Research*, *21*, 1–21. https://doi.org/10.1016/0011-7471(74)90015-1

Warren, B. A. (1978). Bottom water transport through the Southwest Indian ridge. *Deep-Sea Research*, *25*(3), 315–321. https://doi.org/10.1016/0146-6291(78)90596-9

Warren, B. A. (1981). Transindian hydrographic section at lat. 18°S: Property distributions and circulation in the south Indian Ocean. *Deep-Sea Research A*, *28*(8), 759–788. https://doi.org/10.1016/S0198-0149(81)80001-5

Wong, A., Robert, K., & Thierry, C. (2023). Argo quality control manual for CTD and trajectory data—Version 3.7 (Tech. Rep.). https://doi.org/10.13155/33951

Wunsch, C. (1996). *The ocean circulation inverse problem*. Cambridge University Press. https://doi.org/10.1017/CBO9780511629570

You, Y. (2000). Implications of the deep circulation and ventilation of the Indian ocean on the renewal mechanism of North Atlantic deep water. *Journal of Geophysical Research*, *105*(C10), 23895–23926. https://doi.org/10.1029/2000JC900105

Zilberman, N., King, B., Purkey, S., Thierry, V., & Roemmich, D. (2019). Report on the 2nd deep Argo implementation workshop. Hobart, may 13–15th 2019 (Tech. Rep.). Retrieved from https://archimer.ifremer.fr/doc/00507/61873/

Zilberman, N., Roemmich, D., & Gilson, J. (2020). Deep-ocean circulation in the southwest Pacific Ocean interior: Estimates of the mean flow and variability using Deep Argo data. *Geophysical Research Letters*, *47*(13), e2020GL088342. https://doi.org/10.1029/2020GL088342

Zilberman, N., Thierry, V., King, B., Alford, M., André, X., Balem, K., et al. (2023). Observing the full ocean volume using Deep Argo floats. *Frontiers in Marine Science*, *10*. https://doi.org/10.3389/fmars.2023.1287867